Supporting Information

Molecular tunability of surface-functionalized metal nanocrystals for selective electrochemical CO_2 reduction

James R. Pankhurst,[a] Yannick T. Guntern,[a] Mounir Mensi [b] and Raffaella Buonsanti *[a]

[a] Laboratory of Nanochemistry for Energy (LNCE), Institute of Chemical Sciences and Engineering (ISIC), École Polytechnique Fédérale de Lausanne, 1950 Sion, Valais, Switzerland

[b] Institute of Chemical Sciences and Engineering (ISIC), École Polytechnique Fédérale de Lausanne, 1950 Sion, Valais, Switzerland

Table of Contents

Experimental Procedures

Additional general procedures

Fourier-transform infra-red spectra were measured using a Perkin Elmer Spectrum Two FT-IR Spectrometer. Powder samples were placed directly onto and compressed against the ATR sample plate. Air was used as a background measurement and all spectra were recorded with a resolution of 4 cm^{-1}. Assignments are given in the synthesis section, where s = strong absorption, m = medium and w = weak; br = broad absorption band and sh = shoulder.

Direct injection high-resolution mass spectrometry (HRMS) was performed on an QExactive HF Orbitrap-FT-MS instrument, (Thermo Fisher Scientific, Bremen, Germany) coupled to an automated chip-based nanoelectrospray device (Triversa Nanomate, Advion, Ithaca, USA). Electrospray ionization was conducted at a capillary voltage of 1.4 kV and nitrogen nanoflow of 0.15 psi. MS experiments were performed with a nominal resolution of 30,000 and in the positive ion mode.

UV-vis absorption spectra were measured in transmission mode using a Perkin Elmer Lambda 950 Spectrophotometer equipped with a deuterium lamp (for ultra-violet ranges), tungsten halide lamp (for visible and infrared ranges) and a photomultiplier tube (PMT) with a Peltier-cooled PbS detector. Samples were prepared as DMSO or hexane solutions in a quartz cuvette with a 1 cm flight path.

Additional electrochemical procedures

Electrodes were periodically polished with 1 µm diamond paste, and polished regularly in between measurements with 0.05 µm alumina paste (from ALS). After polishing, the electrodes were sonicated twice in Milli-Q water for 10 minutes, and a third time in ethanol before being blown dry under N_2 flow. To prepare the hybrid-catalyst electrodes, Ag-OLAM NCs (OLAM = oleylamine) were first loaded onto the electrode by drop-casting with an Eppendorf 2 – 20 µL pipette, adjusting the stock concentration so that the desired loading could be achieved using a single 10 µL drop (hexane was used as the solvent). The circular area of the catalyst spot was roughly 1.5 cm^2, matching the window in the electrochemical cell (shown in Figure S1). Ligand exchange was then carried out on these films (described below).

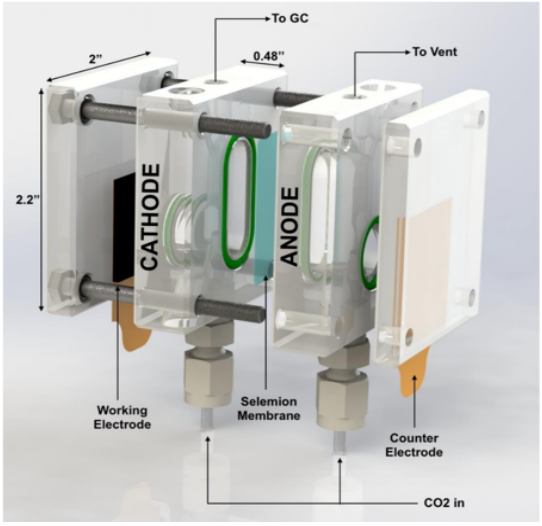

Figure S1. Schematic of the electrochemical cell used for CO_2RR experiments.

Care was taken to avoid contamination of the aqueous electrolyte by trace metals, which can significantly impact the CO_2RR.[1] After machination of the electrochemical cell, it was sonicated in HNO_3 (10% v/v, diluted in milli-Q water) for 15 minutes, and then sonicated and rinsed 5 times in fresh milli-Q water. This process was repeated periodically to remove any Ag material that may have accumulated in the cell from prior experiments. Whilst milli-Q water and high-purity K_2CO_3 (99.995%, Roth AG) were used to prepare the aqueous electrolyte, further purification with Chelex Resin (100 sodium form, 50-100 mesh, dry, Sigma Aldrich) was carried out to remove trace metals. Chelex resin was first stirred over 1 M HCl for 16 hours, decanted and washed with 3 equivalent volumes of water. It was then stirred over 1 M NaOH at 60ºC for 24 hours, decanted and washed with 3 equivalent volumes of water. Finally, the 0.05 M K_2CO_3 electrolyte solution was stirred over the activated resin for 24 hours, and then decanted for use in electrochemistry. Before use in electrochemical experiments, the K_2CO_3 was sparged with CO_2 for 30 minutes to generate 0.1 M $KHCO_3$.

The gas chromatograph (SRI) was calibrated using five calibration gas mixtures (Carbagas, SAPHIR, class 3), spanning 10,000 – 500 ppm for H_2 and 1000 – 100 ppm for CO. Calibration was done with an input gas-flow of 5 sccm and venting gas-flow of 5.5 sccm. A typical experiment to assess the CO_2RR performance includes: 1) verifying that input and venting gas-flow matches that used for calibration; 2) determination of the intrinsic cell resistance by electrochemical impedance spectroscopy; 3) measurement of a linear sweep voltammogram (10 mV s^{-1} under bubbling conditions) to assess the current-response of the catalyst against varying potential; 4) chronoamperometry measurement at a fixed potential, measuring current over time; and 5) measurement of a series of cyclic voltammograms with which to assess the sample capacitance and surface area.

Ohmic drop was determined using potentiometric electrochemical impedance spectroscopy, measuring four spectra at the open-circuit potential, between 1 MHz and 100 Hz, using a sinus amplitude of 20 mV and pause of 0.6 s before each frequency. The value for resistance compensation was taken either from the Nyquist plot (taking the value of Re(Z) at the minimum value of −Im(Z) before the semi-circle), or from the plot of |Z| against frequency, using the asymptotic value of |Z| (Figure S2).

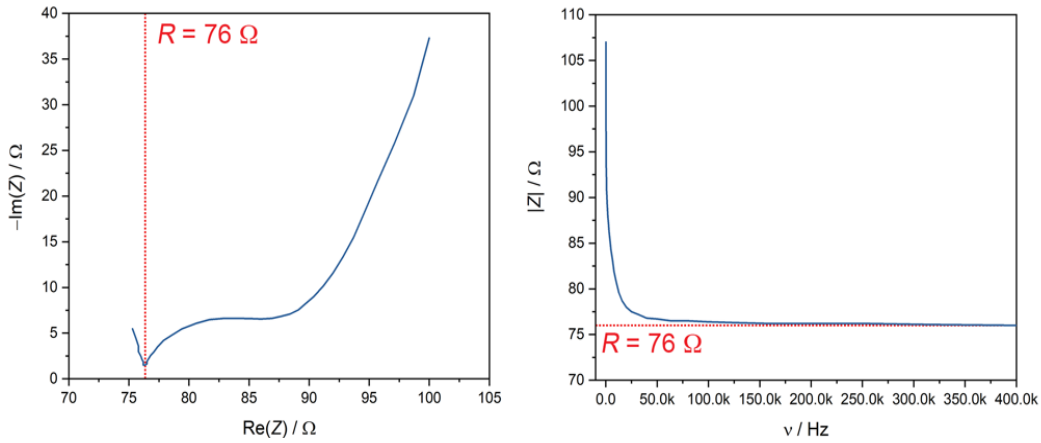

Figure S2. Example plots showing how intrinsic resistance in the electrochemical cell is measured from electrochemical impedance spectroscopy. Left: Nyquist plot, where the resistance value is taken from Re(*Z*) at the minimum value of −Im(*Z*). Right: plot of |*Z*| *vs* frequency; the resistance value is taken as the asymptotic value of |*Z*|.

In order to observe differences between intrinsic catalyst activities, it is essential to normalize currents by the sample surface areas. In our study, we also confirmed that the catalyst morphology does not change drastically between 10 and 85 minutes in the CO_2RR electrolysis, which is the time frame within which we carry out the electrochemical measurements.

After each CO_2RR experiment, all measured currents (I / μA) were normalized by the electrochemically active surface area (S_{ECSA} / cm^2), through measurement of the electrochemical double-layer capacitance (ECDL). To measure the ECDL, cyclic voltammograms (CVs) were first recorded between −0.20 and −0.15 V *vs* Ag/AgCl (in a region where no redox activity takes place) at incremented scan-rates between 4 and 32 mV s^{-1} (Figure S3). The geometric current-density values for the charging (J_c) and discharging (J_d) capacitance were taken at −0.18 V *vs* Ag/AgCl. The difference between these values (J_{total} / μA cm^{-2}) was plotted against the scan rate, ν / V s^{-1}. The slope of this linear plot yields the capacitance value for the sample, C_{sample} / μF cm^{-2}. This process was repeated for a clean Ag foil in order to obtain a reference capacitance value for a flat surface (C_{foil} = 27.8 μF cm^{-2}). Division of C_{sample} by C_{foil} then gives a surface roughness factor (S.R.F.), as in Equation S1. With the S.R.F. value in hand, the geometric surface area of the electrode (S_{geom}, 1.5 cm^2) can be modified to give current density values from the electrochemically active surface area, J_{ECSA} / μA cm^{-2}, as in Equation S2.

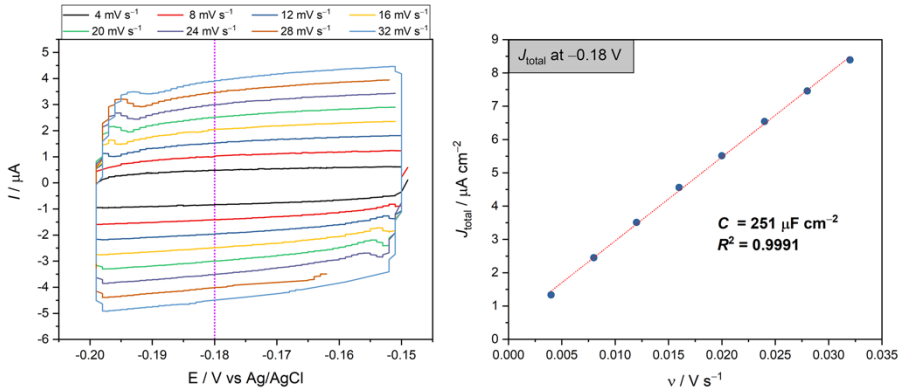

Figure S3. Example plots showing how the sample capacitance is measured, used for normalizing current values by surface area. **Left**: cyclic voltammograms measured in a region where no redox processes or electrocatalysis takes place, at varying scan rates. The vertical pink line highlights the potential at which J_{total} is taken. **Right**: plotting the total current density ($J_{total} = J_{anodic\ scan} - J_{cathodic\ scan}$) against scan rate, where the capacitance is taken from the slope of the linear fit; the geometric surface area is 1.5 cm^2.

$$\text{S.R.F.} = \frac{C_{\text{sample}}}{C_{\text{foil}}}$$

Equation S1

$$J_{\text{ECSA}} = \frac{I}{\text{S.R.F.} \times S_{\text{geom}}}$$

Equation S2

The Faradaic efficiencies for gas products ($FE_{product}$ / %) were calculated according to Equation S3, where R is the gas constant (8.314 J K^{-1} mol^{-1}), T is the temperature (293.15 K), $n_{e,product}$ is the number of electrons required to form the gas product (2 for CO, 2 for H_2), $C_{product}$ is the concentration of gas produced / ppm, F is the Faraday

constant (96,485 C mol^{-1}), I is the average current measured at the time of the GC measurement / A, and t_{fill} is the filling time of the GC (12 seconds). When I > 1 mA in the experiment, the background current and C_{CO}, C_{H2} values (i.e. amounts of products in ppm) from the blank glassy carbon electrode were subtracted in the calculation of FE.

$$\mathrm{FE}_{\mathrm{product}} = \frac{101.325 \times 10^{-9} \times R \times T \times n_{\mathrm{e,product}} \times C_{\mathrm{product}}}{F \times I \times t_{\mathrm{fill}}} \times 100$$

Equation S3

We used the partial current density for CO (J_{CO} / μA cm^{-2}) in order to assess the catalyst activity towards the CO_2RR, as given by Equation S4, where FE_{CO} is the Faradaic efficiency for CO / % and J_{geom} is the geometric current density / μA cm^{-2}.

$$J_{\mathrm{CO}} = \frac{\mathrm{FE}_{\mathrm{CO}} \times J_{\mathrm{geom}} \times S_{\mathrm{geom}}}{100 \times S_{\mathrm{ECSA}}}$$

Equation S4

Specific synthetic procedures

Compound 1-(4-nitrophenyl)imidazole (**1-NO$_2$**) was synthesized using an Ullmann-type reaction adapted from the literature.[2] Compounds 1-(*n*-octyl)imidazole,[3] 1-(*n*-octyl)-2-methylimidazole,[4] 1-(*n*-hexadecyl)imidazole,[5] 1-(triphenylmethyl)imidazole[6] and 1-methyl-3-(4-nitrobenzyl)imidazolium bromide (**2-NO$_2$**)[7] were synthesized according to the methods described below, although we highlight that their syntheses were previously reported elsewhere. Ag foil (0.1 mm, annealed, Premion®, 99.998% metals basis), $AgNO_3$ (99.9995% Puratrem) and benzyl bromide were purchased from ABCR. Oleylamine (technical grade, 70%), *n*-hexylamine, 1-methyl-imidazole, 2-methyl-imidazole, tritylbromide, 4-(methylthio)benzyl bromide, trimethyl oxonium tetrafluoroborate ([Me_3O][BF_4], Meerwein's Salt), cetyltrimethyl ammonium bromide (CTAB) and carbon black (mesoporous graphitized nanopowder, 500 nm particle size by dynamic light-scattering, 99.95% metals basis) were purchased from Sigma Aldrich. Imidazole, *n*-hexadecylbromide, 4-(bromomethyl)benzonitrile and 4-(bromomethyl)benzoic acid were purchased from Fluorochem. 4-(Bromomethyl)nitrobenzene and 1-chloro-4-nitrobenzene were purchased from Acros. *n*-Octylbromide was purchased from TCI. All chemicals were used as supplied without further purification.

Synthesis of 1-(n-octyl)imidazole (Im-3)

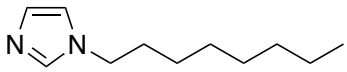

Imidazole (200 mg, 2.94 mmol) was dissolved in a mixture of THF and methanol (100 mL, 7:3 v/v). NaOH (123 mg, 3.09 mmol) was added and the mixture was stirred at room temperature for 1 hour. *n*-Octylbromide (539 mg, 2.79 mmol) was added at room temperature and the mixture was then heated to reflux at 64 ^{o}C; the mixture started to form a precipitate during heating, at 40 ^{o}C. After reflux for 16 hours, the solvent was evaporated, yielding a light red oil mixed with soft crystalline solids. The ^{1}H NMR spectrum of the crude product (d_6-DMSO) revealed that imidazole was still present. The crude product was dissolved in CH_2Cl_2 and washed three times with water to remove NaBr, unreacted NaOH and imidazole. The organic fractions were collected and dried over Na_2SO_4, and then the solvent was evaporated, yielding a colorless oil of much higher purity.

Yield: 376 mg (2.08 mmol, 75%)

^{1}H NMR (d_6-DMSO, 400 MHz), δ_H / ppm: 7.60 (s, 1H, imidazole), 7.14 (s, 1H, imidazole), 6.86 (s, 1H, imidazole), 3.92 (t, 2H, $^{3}J_{HH}$ = 8 Hz, octyl-1 methylene), 1.66 (quintet, 2H, $^{3}J_{HH}$ = 8 Hz, octyl-2 methylene), 1.22 (broad m, 10H, octyl-3,4,5,6,7 methylene), 0.83 (t, 3H, $^{3}J_{HH}$ = 8 Hz, octyl-8 methyl).

Synthesis of 1-(n-octyl)-2-methyl-imidazole (Im-3b)

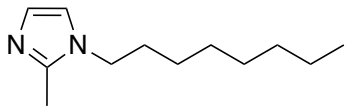

Using the same procedure as for **Im-3**, using 2-methyl-imidazole (3.71 g, 45.2 mmol), NaOH (1.90 g, 47.4 mmol), and *n*-octylbromide (8.28 g, 42.9 mmol) in THF/methanol (150 mL, 1:1 v/v). The mixture turned light orange around 40 ^{o}C and darkened on heating to 60 ^{o}C. After stirring the mixture overnight, a white precipitate had formed. The product was obtained as a brown oil.

Yield: 528 mg (2.72 mmol, 6.3%)

^{1}H NMR (d_6-DMSO, 400 MHz), δ_H / ppm: 7.01 (d, 1H, $^{3}J_{HH}$ = 1.1 Hz, imidazole), 6.69 (d, 1H, $^{3}J_{HH}$ = 1.1 Hz, imidazole), 3.82 (t, 2H, $^{3}J_{HH}$ = 7.2 Hz, octyl-1 methylene), 2.24 (s, 3H, 2-imidazole methyl), 1.62 (quintet, 2H, $^{3}J_{HH}$ = 7.2 Hz, octyl-2 methylene), 1.24 (broad m, 10H, octyl-3,4,5,6,7 methylene), 0.85 (t, 3H, $^{3}J_{HH}$ = 6.8 Hz, octyl-8 methyl).

Synthesis of 1-(n-hexadecyl)imidazole (Im-4)

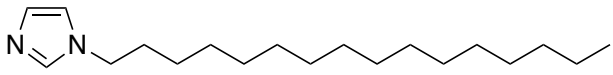

Using the same procedure as for **Im-3**, using imidazole (5.00 g, 73.4 mmol), NaOH (3.08 g, 77.1 mmol), and *n*-hexadecylbromide (21.33 g, 70 mmol) in THF/methanol (200 mL, 7:3 v/v). After heating to 60 ^{o}C, the mixture quickly turned red and deposited white solids on the walls of the flask. The crude product was obtained as a red oil. ^{1}H NMR spectroscopy (C_6D_6) revealed that the desired product had been formed, but unreacted *n*-hexadecylbromide was also present, giving only 63% purity.

In future reactions, the amounts were adjusted in order to limit the amount of unreacted *n*-hexadecylbromide that was formed: imidazole (5.00 g, 73.4 mmol), NaOH (3.23 g, 80.8 mmol), and *n*-hexadecylbromide (13.46 g, 44.1 mmol) in THF/methanol (200 mL, 7:3 v/v). The crude product was a light red oil, but after dissolving in CH_2Cl_2, a yellow solution was formed. After washing three times with water and evaporating the solvent, a light-yellow powder was obtained. ^{1}H NMR spectroscopy (d_6-DMSO) showed that the product from this reaction was of much higher purity (88%).

Yield: 8.0 g (27.35 mmol, 55% based on 88% purity).

^{1}H NMR (d_6-DMSO, 400 MHz), δ_H / ppm: 7.58 (s, 1H, imidazole), 7.13 (s, 1H, imidazole), 6.86 (s, 1H, imidazole), 3.92 (t, 2H, $^3J_{HH}$ = 8 Hz, hexadecyl-1 methylene), 1.67 (quintet, 2H, $^3J_{HH}$ = 8 Hz, hexadecyl-2 methylene), 1.22 (broad s, 26H, hexadecyl-3–15 methylene), 0.85 (t, 3H, $^3J_{HH}$ = 8 Hz, hexadecyl-16 methyl).

Synthesis of 1-(triphenylmethyl)imidazole (Im-5)

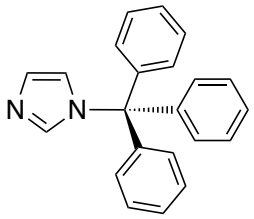

Using the same procedure as for **Im-3**, using imidazole (3.37 g, 49.5 mmol), NaOH (1.98 g, 49.5 mmol), and tritylbromide (4.00 g, 12.4 mmol) in THF/methanol (150 mL, 7:3 v/v). The mixture was stirred at room temperature for 3 hours, turning yellow and forming a small amount of a white precipitate. Heating to 60 ^{o}C and stirring overnight turned the mixture orange. After extraction by CH_2Cl_2, yellow crystalline solids were obtained on evaporation of the solvent. In the ^{1}H NMR spectrum of the crude product, lots of trityl bromide was observed. Acetone was stirred over the crude product, and the yellow supernatant was decanted, leaving the product in the residues as a white crystalline solid.

Yield: 950 mg (3.06 mmol, 25%).

^{1}H NMR (d_6-benzene, 400 MHz), δ_H / ppm: 7.63 (s, 1H, imidazole), 7.27 (s, 1H, imidazole), 7.09 – 7.04 (m, 6H, *ortho*-phenyl), 6.98 – 6.92 (m, 9H, *meta*- and *para*-phenyl), 6.69 (s, 1H, imidazole).

Synthesis of 1-methyl-3-(4-nitrobenzyl)imidazolium bromide (2-NO$_2$)

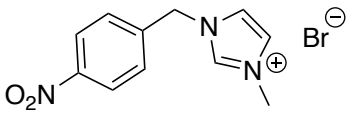

A light yellow solution of 4-(bromomethyl)nitrobenzene (2631 mg, 12.18 mmol) in acetone (7 mL) was stirred in a vial. A second solution of 1-(methyl)imidazole (1000 mg, 12.18 mmol) in acetone (2 mL) was added in a single portion. Needle-shaped crystalline solids formed within 30 minutes of stirring. After 2 hours, the solids were separated by centrifugation, and then they were washed once with clean acetone and a second time with hexane, decanting the supernatant by centrifugation each time. The colourless, crystalline solids were then dried at 70 ^{o}C.

Yield: 660 mg (2.21 mmol, 18%). High mass loss likely comes from washing in acetone.

^{1}H NMR (d_6-DMSO, 400 MHz), δ_H / ppm: 9.31 (s, 1H, imidazole-2), 8.28 (d, 2H, $^3J_{HH}$ = 8.7 Hz, phenyl), 7.85 (t*, 1H, $^3J_{HH}$ = 1.7 Hz, imidazole-4 or -5), 7.78 (t*, 1H, $^3J_{HH}$ = 1.7 Hz, imidazole-4 or -5), 7.68 (d, 2H, $^3J_{HH}$ = 8.7 Hz, phenyl), 5.63 (s, 2H, benzyl), 3.88 (s, 3H, methyl). *n.b. the apparent triplet multiplicity is assigned to poorly-resolved overlapping doublet-of-doublet resonances, where each 4/5-imidazole proton couples to the remaining two protons within the heterocycle. This was an occurring pattern for all asymmetrically disubstituted imidazolium compounds reported here.

Synthesis of 1-(n-octyl)-3-(4-cyanobenzyl)imidazolium bromide (3-CN)

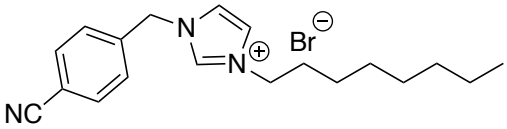

A colourless solution of 4-(bromomethyl)benzonitrile (1087 mg, 5.55 mmol) in acetone (10 mL) was stirred in a vial. A second solution of **Im-3** (1000 mg, 5.55 mmol) in acetone (2 mL) was drop-wise added. No changes were observed during the addition. The solution was stirred for 6 hours, during which time the solution turned very light brown. Evaporation of the solvent yielded a light orange oil that solidified into an off-white, gummy solid after a few hours. The solid was washed by stirring once in 9:1 hexane/acetone, and a second time in hexane, isolating the solids by centrifugation in each case. The product was isolated as a free-flowing white powder that was dried at 70 ^{o}C.

Yield: 1426 mg (3.79 mmol, 68%).

^{1}H NMR (d_6-DMSO, 400 MHz), δ_H / ppm: 9.49 (s, 1H, imidazole-2), 7.92 – 7.89 (m, 4H; overlapping resonances from 2 phenyl protons and 2 protons in imidazole-4 and -5 positions), 7.63 (d, 2H, $^3J_{HH}$ = 8.2 Hz, phenyl), 5.60 (s, 2H, benzyl), 4.19 (t, 2H, $^3J_{HH}$ = 7.2 Hz, octyl-1 methylene), 1.79 (quintet, 2H, $^3J_{HH}$ = 7.2 Hz, octyl-2 methylene), 1.27 – 1.18 (m, 10H, octyl-3,4,5,6,7 methylene), 0.83 (t, 3H, $^3J_{HH}$ = 6.8 Hz, octyl-8 methyl).

^{13}C{^{1}H} NMR (d_6-DMSO, 100.6 MHz, assignments based on HSQC correlation with ^{1}H NMR), δ_C / ppm: 140.2 (phenyl 4^o), 136.4 (imidazole-2), 132.8 (phenyl), 129.1 (phenyl), 122.9 (imidazole-4 or -5), 122.6 (imidazole-4 or -5), 118.3 (nitrile), 111.4 (phenyl 4^o), 51.2 (benzyl), 49.1 (octyl-1), 31.0 (octyl-3 to -7), 29.1 (octyl-2), 28.4 (octyl-3 to -7), 28.2 (octyl-3 to -7), 25.4 (octyl-3 to -7), 22.0 (octyl-3 to -7), 13.8 (octyl-8 methyl).

FT-IR (ATR plate), ν / cm^{-1}: 3405 s, br (water), 3130 w, 3067 w, 2954 sh, 2927 m, 2856 m, 2230 m (nitrile CN stretch), 1611 w, 1559 m, 1507 w, 1457 m, 1414 w, 1361 w, 1331 w, 1209 w, 1155 s, 1121 w, 1022 m, 858 w, 825 m, 764 m, 691 w, 636 w, 611 w, 552 s.

HRMS (nanochip ESI), *m*/*z*: $[M]^+$ calculated for $C_{19}H_{26}N_3^+$ 296.2121, found 296.2115. Also observed the halide-bridged dimer $[(C_{19}H_{26}N_3)_2Br]^+$ at 672 *m*/*z*.

Synthesis of 1-(n-octyl)-3-(4-nitrobenzyl)imidazolium bromide (3-NO_2)

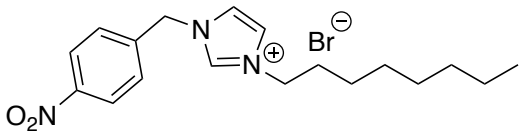

A light yellow solution of 4-(bromomethyl)nitrobenzene (11.98 g, 55.5 mmol) in acetone (35 mL) was stirred in a vial. A second solution of **Im-3** (10.00 g, 55.5 mmol) in acetone (15 mL) was drop-wise added. No changes were observed during the addition or during overnight stirring. Evaporation of the solvent in an evaporating dish yielded a yellow oil, which produced large block crystals after standing for 1 week. The crude product appears to have high purity from ^{1}H NMR spectroscopy, but washing was carried out to ensure removal of any unreacted starting material. The yellow, oily solids were suspended and stirred in 9:1 hexane/acetone, and then again in hexane; the solids were recollected by centrifugation in each case. The oily consistency was still evident after washing, although the dark yellow colour was removed. Drying of the semi-crystalline material at 70 ^{o}C caused the crystals to melt into a light-yellow oil.

Yield: 19.02 g (48 mmol, 86%).

Additional information on the purification: crystallisation from acetone / hexane mixtures was not successful, as the surfactant properties of **3-NO_2** create an emulsion. The crystals of **3-NO_2** can be washed quickly with pure acetone, but this sacrifices a significant amount of material with no additional gain in purity, and without removal of the yellow colour or oily consistency.

^{1}H NMR (d_6-DMSO, 400 MHz), δ_H / ppm: 9.45 (s, 1H, imidazole-2), 8.28 (d, 2H, $^3J_{HH}$ = 8.7 Hz, phenyl), 7.89 (t, 2H, $^3J_{HH}$ = 1.7 Hz, imidazole-4,5), 7.69 (d, 2H, $^3J_{HH}$ = 8.7 Hz, phenyl), 5.64 (s, 2H, benzyl), 4.19 (t, 2H, $^3J_{HH}$ = 7.3 Hz, octyl-1 methylene), 1.80 (quintet, 2H, $^3J_{HH}$ = 7.3 Hz, octyl-2 methylene), 1.29 – 1.19 (m, 10H, octyl-3,4,5,6,7 methylene), 0.84 (t, 3H, $^3J_{HH}$ = 7.3 Hz, octyl-8 methyl).

^{13}C{^{1}H} NMR (d_6-DMSO, 100.6 MHz, assignments based on HSQC correlation with ^{1}H NMR), δ_C / ppm: 147.6 (phenyl 4^o), 142.1 (phenyl 4^o), 136.5 (imidazole-2), 129.5 (phenyl C–H), 123.9 (phenyl C–H), 122.9 (imidazole-4 or -5), 122.7 (imidazole-4 or -5), 50.9 (benzyl), 49.0 (octyl-1), 31.0 (octyl-3 to -7), 29.2 (octyl-2), 28.4 (octyl-3 to -7), 28.2 (octyl-3 to -7), 25.4 (octyl-3 to -7), 22.0 (octyl-3 to -7), 13.8 (octyl-8 methyl).

FT-IR (ATR plate), ν / cm^{-1}: 3412 br, s (water), 3129 w, 3061 w, 2952 sh, 2926 m, 2856 m, 1607 w, 1560 m, 1520 s (nitro N-O stretch), 1457 m, 1346 s (nitro N-O stretch), 1154 s, 1109 m, 1017 w, 858 m, 805 m, 721 s, 652 w, 613 w, 528 w, 475 w.

HRMS (nanochip ESI), *m*/*z*: $[M]^+$ calculated for $C_{18}H_{26}N_3O_2^+$ 316.2020, found 316.2014. Also observed the halide-bridged dimer $[(C_{18}H_{26}N_3O_2)_2Br]^+$ at 711 *m*/*z*.

Synthesis of 1-(n-octyl)-2-methyl-3-(4-nitrobenzyl)imidazolium bromide (3b-NO_2)

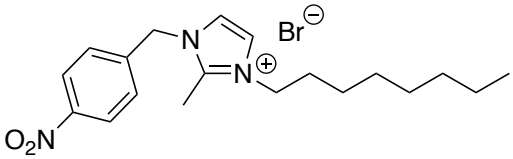

4-(bromomethyl)nitrobenzene (222 mg, 1.03 mmol) was added to a light brown solution of **Im-3b** (200 mg, 1.03 mmol) in acetone (5 mL), quickly forming a solution. After 2 hours of stirring, a white precipitate had formed. The

mixture was stirred for an additional hour, and then centrifuged at 5000 rpm for 10 mins; the brown supernatant was decanted and the white solids were dried at 60 °C.

Yield: 280 mg (0.68 mmol, 66%).

^{1}H NMR (d_6-DMSO, 400 MHz), δ_H / ppm: 8.27 (d, 2H, $^3J_{HH}$ = 8.7 Hz, phenyl), 7.81 (m, 2H, imidazole-4,5), 7.58 (d, 2H, $^3J_{HH}$ = 8.7 Hz, phenyl), 5.62 (s, 2H, benzyl), 4.12 (t, 2H, $^3J_{HH}$ = 7.4 Hz, octyl-1 methylene), 2.61 (s, 3H, imidazole-2 methyl), 1.73 (quintet, 2H, $^3J_{HH}$ = 7.3 Hz, octyl-2 methylene), 1.26 – 1.24 (broad m, 10H, octyl-3,4,5,6,7 methylene), 0.85 (t, 3H, $^3J_{HH}$ = 7.3 Hz, octyl-8 methyl).

^{13}C{^{1}H} NMR (d_6-DMSO, 100.6 MHz, assignments based on HSQC correlation with ^{1}H NMR), δ_C / ppm: 147.4 (phenyl 4°), 144.6 (phenyl 4°), 142.0 (imidazole-2), 129.0 (phenyl C–H), 124.0 (phenyl C–H), 121.8 (imidazole-4 and -5), 49.8 (benzyl), 47.8 (octyl-1), 31.2 (octyl-3 to -7), 29.0 (octyl-2), 28.5 (octyl-3 to -7), 28.5 (octyl-3 to -7), 25.6 (octyl-3 to -7), 22.1 (octyl-3 to -7), 14.0 (octyl-8 methyl), 9.6 (imidazole-2 methyl).

FT-IR (ATR plate), ν / cm^{-1}: 3064 w, 2926 m, 2850 w, 1602 w, 1588 w, 1512 s (nitro N-O stretch), 1462 m, 1424 w, 1392 w, 1338 s (nitro N-O stretch), 1262 m, 1248 w, 1214 w, 1190 w, 1168 w, 1130 w, 1106 m, 1066 w, 1038 w, 1016 w, 960 w, 894 w, 880 w, 856 s, 822 w, 808 m, 778 w, 744 s, 738 s, 726 m, 694 w, 670 m, 640 m, 628 w, 610 w, 526 w, 510 w, 472 m.

HRMS (nanochip ESI), *m*/*z*: $[M]^+$ calculated for $C_{19}H_{28}N_3O_2^+$ 330.2181, found 330.2178.

Synthesis of 1-(n-octyl)-3-(4-carboxybenzyl)imidazolium bromide (3-CO_2H)

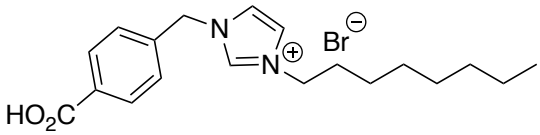

A light yellow suspension of 4-(bromomethyl)benzoic acid (955 mg, 4.44 mmol) in acetone (10 mL) was stirred in a vial. A second solution of **Im-3** (800 mg, 4.44 mmol) in acetone (2 mL) was drop-wise added. The suspension quickly turned white, then clear and colorless, and finally turned light yellow and clear at the end of the addition. After stirring for 6 hours, white solids precipitated from the solution. The solvent was evaporated overnight in an evaporating dish, yielding a waxy white solid. The ^{1}H NMR spectrum of the crude product was found to contain two products. The crude product was precipitated from an ethanol solution layered with hexane in the refrigerator, yielding a white powder that consisted of a single compound by ^{1}H NMR spectroscopy.

Yield: 540 mg (1.37 mmol, 31%).

As an alternative work-up, the white precipitate from the reaction (using 5.55 mmol of each reagent) was collected by centrifugation, discarding the acetone supernatant. The solids were then washed once by stirring over clean acetone and a second time with hexane, collecting the white solids each time by centrifugation. The final product was dried at 70 °C.

Yield: 1418 mg (3.59 mmol, 65%).

^{1}H NMR (d_6-DMSO, 400 MHz), δ_H / ppm: 9.42 (s, 1H, imidazole-2), 7.97 (d, 2H, $^3J_{HH}$ = 8 Hz, phenyl C–H, *ortho*- to acid), 7.88 (s, 2H, imidazole-4,5), 7.52 (d, 2H, $^3J_{HH}$ = 8 Hz, phenyl C–H, *meta*- to acid), 5.55 (s, 2H, benzyl), 4.18 (t, 2H, $^3J_{HH}$ = 7.2 Hz, octyl-1 methylene), 3.37 (broad s, 1H, CO_2H), 1.79 (quintet, 2H, $^3J_{HH}$ = 7.2 Hz, octyl-2 methylene), 1.27 – 1.17 (m, 10 H, octyl-3,4,5,6,7 methylene), 0.84 (t, 3H, $^3J_{HH}$ = 6.6 Hz, octyl-8 methyl).

$^{13}C\{^1H\}$ NMR (d_6-DMSO, 100.6 MHz, assignments based on HSQC correlation with ^1H NMR), δ_C / ppm: 166.9 (CO_2H), 139.6 (phenyl 4°, next to CO_2H), 136.4 (imidazole-2), 131.0 (phenyl 4°, *para*- to CO_2H), 129.9 (phenyl C–H, *ortho*- to CO_2H), 128.4 (phenyl C–H, *meta*- to CO_2H), 122.9 (imidazole-4 or -5), 122.8 (imidazole-4 or -5), 51.5 (benzyl), 49.0 (octyl-1), 31.2 (octyl-3 to -7), 29.3 (octyl-2), 28.5 (octyl-3 to -7), 28.3 (octyl-3 to -7), 25.5 (octyl-3 to -7), 22.1 (octyl-3 to -7), 14.0 (octyl-8 methyl).

FT-IR (ATR plate), ν / cm^{-1}: 3140 w, 3084 w, 3030 w, 2920 m, 2855 m, 1706 s, 1614 w, 1562 m, 1448 w, 1422 w, 1377 m, 1278 w, 1223 s, 1167 m, 1168 s, 1015 w, 852 w, 816 m, 764 sh, 740 s, 632 m, 610 s, 516 w, 474 w.

HRMS (nanochip ESI), *m*/*z*: $[M]^+$ calculated for $C_{19}H_{27}N_2O_2^+$ 315.2067, found 315.2063.

Synthesis of 1-(n-octyl)-3-{4-(methylthio)benzyl}imidazolium bromide (3-SCH$_3$)

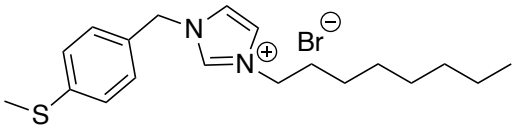

A colorless suspension of 4-(methylthio)benzyl bromide (672 mg, 3.1 mmol) in acetone (6 mL) was stirred in a vial. A second solution of **Im-3** (558 mg, 3.1 mmol) in acetone (1 mL) was drop-wise added. No changes were observed during the addition. The solution was stirred for 6 hours, over which time the solution turned very light brown. Evaporation of the solvent yielded a dark brown, viscous oil that was washed by suspending in 9:1 hexane/acetone and then collected by centrifugation. Solvent was removed from the oil by heating at 70 °C.

Yield: 449 mg (1.42 mmol, 36%).

^1H NMR (d_6-DMSO, 400 MHz), δ_H / ppm: 9.49 (t, 1H, J_{HH} = 1.6 Hz, imidazole-2), 7.88, 7.86 (two overlapping triplets, total of 2H, J_{HH} = 1.6 Hz, imidazole-4,5), 7.43 (d, 2H, $^3J_{HH}$ = 8.3 Hz, phenyl), 7.27 (d, 2H, $^3J_{HH}$ = 8.3 Hz, phenyl), 5.43 (s, 2H, benzyl), 4.18 (t, 2H, $^3J_{HH}$ = 7.2 Hz, octyl-1 methylene), 2.45 (s, 3H, thiomethyl), 1.77 (quintet, 2H, $^3J_{HH}$ = 7.2 Hz, octyl-2 methylene), 1.25 – 1.15 (m, 10H, octyl-3,4,5,6,7 methylene), 0.82 (t, 3H, $^3J_{HH}$ = 6.8 Hz, octyl-8 methyl).

$^{13}C\{^1H\}$ NMR (d_6-DMSO, 100.6 MHz, assignments based on HSQC and HMBC correlation with ^1H NMR), δ_C / ppm: 139.3 (phenyl 4°, C–S), 136.0 (imidazole-2), 131.3 (phenyl 4°, *para*- to SMe), 129.2 (phenyl C–H, *ortho*- to SMe), 126.0 (phenyl C–H, *meta*- to SMe), 122.8 (imidazole C–H, nearest benzyl), 122.5 (imidazole C–H, nearest alkyl), 51.4 (benzyl), 49.0 (octyl-1), 32.2 (octyl-7), 29.4 (octyl-2), 28.6 (octyl-4), 28.4 (octyl-5), 25.6 (octyl-3), 22.2 (octyl-6), 14.5 (thiomethyl), 14.0 (octyl-8 methyl).

FT-IR (ATR plate), ν / cm^{-1}: 3414 br, s (water), 3129 w, 3068 w, 2954 sh, 2924 s, 2855 m, 1626 w, 1601 w, 1558 s, 1496 s, 1456 m, 1409 w, 1357 w, 1326 w, 1154 s, 1091 m, 1017 w, 955 w, 842 w, 814 m, 752 s, 668 w, 615 w, 502 w.

HRMS (nanochip ESI), *m*/*z*: $[M]^+$ calculated for $C_{19}H_{29}N_2S^+$ 317.2045, found 317.2057.

Synthesis of 1-(n-octyl)-3-(benzyl)imidazolium bromide (3-H)

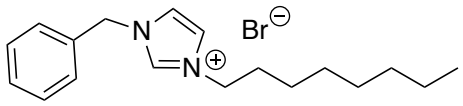

A colorless solution of benzyl bromide (949 mg, 5.55 mmol) in acetone (6 mL) was stirred in a vial. A second solution of **Im-3** (1000 mg, 5.55 mmol) in acetone (1 mL) was drop-wise added. No changes were observed during the addition. The solution was stirred for 6 hours, over which time the solution turned very light brown. The solvent was evaporated at 70 °C, yielding a light orange oil. Neither trituration with hexane, nor cooling in the refrigerator yielded any solids from the oil.

Yield: 1920 mg (5.46 mmol, 98%).

^{1}H NMR (d_6-DMSO, 400 MHz), δ_H / ppm: 9.44 (s, 1H, imidazole-2), 7.86, 7.85 (m, 2H, overlapping imidazole-4,5), 7.45 – 7.38 (m, 5H, phenyl), 5.46 (s, 2H, benzyl), 4.18 (t, 2H, $^3J_{HH}$ = 7.2 Hz, octyl-1 methylene), 1.79 (quintet, 2H, $^3J_{HH}$ = 7.2 Hz, octyl-2 methylene), 1.22 (broad m, 10H, octyl-3,4,5,6,7 methylene), 0.84 (t, 3H, $^3J_{HH}$ = 6.8 Hz, octyl-8 methyl).

^{13}C{^{1}H} NMR (d_6-DMSO, 100.6 MHz, assignments based on HSQC correlation with ^{1}H NMR), δ_C / ppm: 136.1 (imidazole-2), 135.0 (phenyl 4°-C), 129.0 (phenyl C–H), 128.7 (phenyl *para*-H), 128.3 (phenyl C–H), 122.8 (imidazole-4/5), 122.6 (imidazole-4/5), 51.9 (benzyl), 49.0 (octyl-1), 31.1 (octyl-7), 29.2 (octyl-2), 28.5 (octyl-4), 28.3 (octyl-5), 25.5 (octyl-3), 22.0 (octyl-6), 13.9 (octyl-8 methyl).

FT-IR (ATR plate), ν / cm^{-1}: 3414 br, s (water), 3133 w, 3066 m, 3038 sh, 2955 s, 2927 s, 2856 s, 1625 m, 1562 s, 1499 w, 1460 s, 1408 w, 1377 w, 1360 w, 1329 w, 1206 w, 1155 s, 1080 w, 1028 w, 866 w, 823 m, 712 s, 645 w, 613 w, 569 w, 462 m.

HRMS (nanochip ESI), *m*/*z*: $[M]^+$ calculated for $C_{18}H_{27}N_2^+$ 271.2169, found 271.2168.

Synthesis of 1-(n-hexadecyl)-3-(4-cyanobenzyl)imidazolium bromide (4-CN)

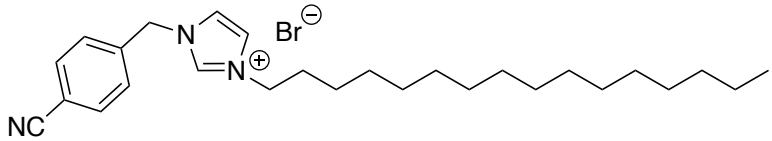

To a colourless solution of 4-(bromomethyl)benzonitrile (500 mg, 2.55 mmol) in acetone (3 mL) was added **Im-4** (848 mg, 2.55 mmol based on 88% purity). The solution quickly turned yellow and was stirred for 2 hours, after which time the solvent was evaporated, yielding a light-yellow solid. This crude product was found to contain an impurity by ^{1}H NMR spectroscopy, evident from an extra triplet resonance at 3.28 ppm (d_6-DMSO) corresponding to the hexadecyl-1 position, as well as unexpectedly large integration of the broad singlet at 1.23 ppm, which represents the majority of the methylene protons in the hydrocarbon chain. However, this side product can be removed by washing. The crude product was suspended in hexane (20 mL) and centrifuged, discarding the light-yellow hexane supernatant; this was repeated three times, resulting in a white, free-flowing solid that was dried at 70 °C.

Yield: 975 mg (2.00 mmol, 78%).

^{1}H NMR (d_6-DMSO, 400 MHz), δ_H / ppm: 9.32 (s, 1H, imidazole-2), 7.92 (d, 2H, $^3J_{HH}$ = 8.3 Hz, phenyl), 7.84 (m, 2H, imidazole-4,5), 7.58 (d, 2H, $^3J_{HH}$ = 8.2 Hz, phenyl), 5.54 (s, 2H, benzyl), 4.17 (t, 2H, $^3J_{HH}$ = 7.0 Hz,

hexadecyl-1 methylene), 1.78 (quintet, 2H, $^3J_{HH}$ = 7.0 Hz, hexadecyl-2 methylene), 1.28 – 1.19 (m, 26H, hexadecyl-3–15 methylene), 0.85 (t, 3H, $^3J_{HH}$ = 7.0 Hz, hexadecyl-16 methyl).

^{13}C{^{1}H} NMR (d_6-DMSO, 100.6 MHz), δ_C / ppm: 140.3 (imidazole-2), 136.5 (*ipso*-phenyl), 132.9 (phenyl C–H), 129.1 (phenyl C–H), 123.0 (imidazole-4 or -5), 122.7 (imidazole-4 or -5), 118.4 (nitrile), 111.5 (*ipso*-phenyl), 51.3 (benzyl), 49.0 (hexadecyl-1), 31.3 (hexadecyl-2–14), 29.2 (hexadecyl-2–14), 29.1 (hexadecyl-2–14), 29.0 (hexadecyl-2–14), 28.9 (hexadecyl-2–14), 28.8 (hexadecyl-2–14), 28.7 (hexadecyl-2–14), 28.4 (hexadecyl-2–14), 25.5 (hexadecyl-2–14), 22.1 (hexadecyl-15), 14.0 (hexadecyl-16).

FT-IR (ATR plate), ν / cm^{-1}: 2918 s, 2849 s, 2236 m (nitrile CN stretch), 1613 w, 1560 m, 1509 w, 1468 m, 1417 w, 1345 w, 1209 w, 1162 s, 1108 w, 1026 w, 859 m, 817 m, 759 m, 720 m, 691 w, 628 m, 547 s, 454 w.

HRMS (nanochip ESI), *m*/*z*: $[M]^+$ calculated for $C_{27}H_{42}N_3^+$ 408.3371, found 408.3373.

Synthesis of 1-(n-hexadecyl)-3-(4-nitrobenzyl)imidazolium bromide (4-NO$_2$)

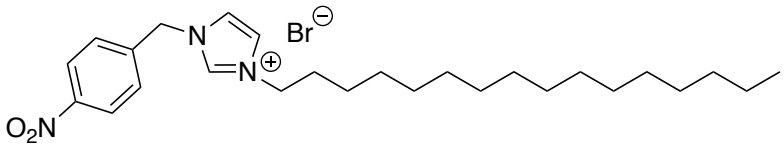

The same procedure was followed as for above, using: 4-(bromomethyl)nitrobenzene (500 mg, 2.31 mmol) in acetone (3 mL) and **Im-4** (769 mg, 2.31 mmol based on 88% purity). The solution also quickly turned yellow and gave an off-white powder on evaporation of the solvent. Three washes with hexane (20 mL) produced a free-flowing white powder that was dried at 70 ^{o}C.

Yield: 990 mg (1.95 mmol, 84%).

^{1}H NMR (d_6-DMSO, 400 MHz), δ_H / ppm: 9.38 (s, 1H, imidazole-2), 8.28 (d, 2H, $^3J_{HH}$ = 8.7 Hz, phenyl), 7.87 (s, 1H, imidazole-4 or -5), 7.87 (s, 1H, imidazole-4 or -5), 7.67 (d, 2H, $^3J_{HH}$ = 8.7 Hz, phenyl), 5.62 (s, 2H, benzyl), 4.18 (t, 2H, $^3J_{HH}$ = 7.2 Hz, hexadecyl-1 methylene), 1.79 (quintet, 2H, $^3J_{HH}$ = 7.2 Hz, hexadecyl-2 methylene), 1.23 (broad s, 26H, hexadecyl-3–15 methylene), 0.85 (t, 3H, $^3J_{HH}$ = 7.2 Hz, hexadecyl-16 methyl).

^{13}C{^{1}H} NMR (d_6-DMSO, 100.6 MHz), δ_C / ppm: 147.6 (*ipso*-phenyl), 142.2 (imidazole-2), 136.6 (*ipso*-phenyl), 129.5 (phenyl C–H), 124.0 (phenyl C–H), 123.0 (imidazole-4 or -5), 122.7 (imidazole-4 or -5), 51.0 (benzyl), 49.1 (hexadecyl-1), 31.3 (hexadecyl-2–14), 29.2 (hexadecyl-2–14), 29.1 (hexadecyl-2–14), 29.0 (hexadecyl-2–14), 28.9 (hexadecyl-2–14), 28.8 (hexadecyl-2–14), 28.7 (hexadecyl-2–14), 28.4 (hexadecyl-2–14), 25.5 (hexadecyl-2–14), 22.1 (hexadecyl-15), 14.0 (hexadecyl-16).

FT-IR (ATR plate), ν / cm^{-1}: 3060 w, 2960 m, 2916 s, 2850 s, 1600 w, 1576 w, 1560 w, 1513 s (nitro N-O stretch), 1470 s, 1400 w, 1342 s (nitro N-O stretch), 1273 w, 1221 w, 1168 s, 1104 m, 1014 w, 976 w, 944 w, 897 w, 859 w, 836 m, 800 w, 762 s, 735 s, 720 s, 674 w, 621 s.

HRMS (nanochip ESI), *m*/*z*: $[M]^+$ calculated for $C_{26}H_{42}N_3O_2^+$ 428.3271, found 428.3272

Synthesis of 1-(n-hexadecyl)-3-(4-carboxybenzyl)imidazolium bromide (4-CO_2H)

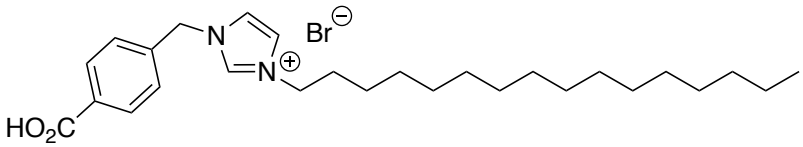

The same procedure was followed as for above, using: 4-(bromomethyl)benzoic acid (500 mg, 2.32 mmol) in acetone (3 mL) and **Im-4** (773 mg, 2.32 mmol based on 88% purity). The cloudy suspension of the acid in acetone quickly turned clear and yellow after addition of the imidazole. An off-white powder was obtained on evaporation of the solvent. Three washes with hexane (20 mL) produced a free-flowing white powder that was dried at 70 °C; in this case not all of the side-product could be removed by washing with hexane. Further purification is possible by dissolving the product in the minimum volume of hot ethanol (at 70 °C), leaving to cool to room temperature, and then carefully layering the ethanol solution with hexane; on standing at 4 °C, a white powder precipitates at the ethanol/hexane interface that is of higher purity.

Yield: 829 mg (1.63 mmol, 70%).

^{1}H NMR (d_6-DMSO, 400 MHz), δ_H / ppm: 9.37 (s, 1H, imidazole-2), 7.97 (d, 2H, $^3J_{HH}$ = 8.2 Hz, phenyl), 7.86 (s, 1H, imidazole-4 or -5), 7.85 (s, 1H, imidazole-4 or -5), 7.50 (d, 2H, $^3J_{HH}$ = 8.2 Hz, phenyl), 5.53 (s, 2H, benzyl), 4.18 (t, 2H, $^3J_{HH}$ = 7.2 Hz, hexadecyl-1 methylene), 3.36 (broad s, water and -CO_2H), 1.77 (quintet, 2H, $^3J_{HH}$ = 7.2 Hz, hexadecyl-2 methylene), 1.22 (broad s, 26H, hexadecyl-3–15 methylene), 0.84 (t, 3H, $^3J_{HH}$ = 6.8 Hz, hexadecyl-16 methyl).

^{13}C{^{1}H} NMR (d_6-DMSO, 100.6 MHz), δ_C / ppm: 166.8 (-CO_2H), 139.6 (imidazole-2), 136.4 (*ipso*-phenyl, next to benzyl), 131.0 (*ipso*-phenyl, next to -CO_2H), 129.9 (phenyl C–H), 128.3 (phenyl C–H), 122.9 (imidazole-4 or -5), 122.7 (imidazole-4 or -5), 51.5 (benzyl), 49.0 (hexadecyl-1), 31.3 (hexadecyl-2–14), 29.2 (hexadecyl-2–14), 29.1 (hexadecyl-2–14), 29.0 (hexadecyl-2–14), 28.9 (hexadecyl-2–14), 28.8 (hexadecyl-2–14), 28.7 (hexadecyl-2–14), 28.3 (hexadecyl-2–14), 25.5 (hexadecyl-2–14), 22.1 (hexadecyl-15), 14.0 (hexadecyl-16).

FT-IR (ATR plate), ν / cm^{-1}: 3164 – 2710 br (carboxylic acid O-H stretch), 2916 s, 2850 s, 1708 s (carboxylic acid C=O stretch), 1615 w, 1556 m, 1472 m, 1418 m, 1374 m, 1282 w, 1217 s, 1158 s, 1110 s, 1022 w, 840 m, 764 m, 741 s, 719 m, 646 w, 612 s, 517 w, 468 w.

HRMS (nanochip ESI), *m*/*z*: $[M]^+$ calculated for $C_{27}H_{43}N_2O_2^+$ 427.3310, found 427.3319

Synthesis of 1-(n-hexadecyl)-3-{4-(methylthio)benzyl}imidazolium bromide (4-SCH_3)

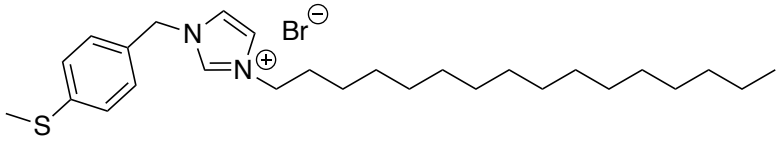

The same procedure was followed as for above, using: 4-(methylthio)benzyl bromide (500 mg, 2.30 mmol) in acetone (3 mL) and **Im-4** (766 mg, 2.30 mmol based on 88% purity). The solution quickly turned yellow and cloudy, and gave an off-white powder on evaporation of the solvent. Three washes with hexane (20 mL) produced a gummy tan solid that melted during drying at 70 °C.

Yield: 734 mg (1.44 mmol, 63%).

^{1}H NMR (d_6-DMSO, 400 MHz), δ_H / ppm: 9.39 (s, 1H, imidazole-2), 7.84 (appears as a quintet, 2H, imidazole-4,5), 7.40 (d, 2H, $^3J_{HH}$ = 8.4 Hz, phenyl), 7.29 (d, 2H, $^3J_{HH}$ = 8.4 Hz, phenyl), 5.40 (s, 2H, benzyl), 4.17 (t, 2H, $^3J_{HH}$

= 7.0 Hz, hexadecyl-1 methylene), 2.46 (s, 3H, S-CH_3), 1.77 (quintet, 2H, $^3J_{HH}$ = 7.3 Hz, hexadecyl-2 methylene), 1.22 (s, 26H, hexadecyl-3–15 methylene), 0.84 (t, 3H, $^3J_{HH}$ = 7.3 Hz, hexadecyl-16 methyl).

$^{13}C\{^1H\}$ NMR (d_6-DMSO, 100.6 MHz), δ_C / ppm: 139.2 (imidazole-2), 136.0 (*ipso*-phenyl), 131.2 (*ipso*-phenyl), 129.1 (phenyl C–H), 126.1 (phenyl C–H), 122.8 (imidazole-4 or -5), 122.4 (imidazole-4 or -5), 51.4 (benzyl), 48.9 (hexadecyl-1), 31.3 (hexadecyl-2–14), 29.3 (hexadecyl-2–14), 29.1 (hexadecyl-2–14), 29.0 (hexadecyl-2–14), 28.9 (hexadecyl-2–14), 28.8 (hexadecyl-2–14), 28.7 (hexadecyl-2–14), 28.3 (hexadecyl-2–14), 25.5 (hexadecyl-2–14), 22.1 (hexadecyl-15), 14.5 (S-CH_3), 14.0 (hexadecyl-16).

FT-IR (ATR plate), ν / cm^{-1}: 3036 w, 2916 s, 2849 s, 1557 m, 1494 w, 1464 m, 1440 w, 1405 w, 1368 w, 1150 s, 1092 w, 1017 w, 956 w, 886 w, 842 m, 808 m, 751 s, 719 m, 660 w, 635 m, 616 w, 501 m.

HRMS (nanochip ESI), *m*/*z*: $[M]^+$ calculated for $C_{27}H_{45}N_2S^+$ 429.3298, found 429.3294

Synthesis of 1-(triphenylmethyl)-3-(4-nitrobenzyl)imidazolium bromide (5-NO_2)

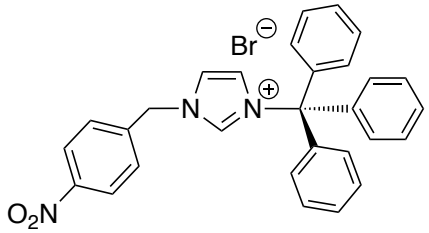

To a solution of 4-(bromomethyl)nitro benzene (139 mg, 0.64 mmol) in toluene (7 mL) was added **Im-5** (200 mg, 0.64 mmol), initially forming a suspension before the imidazole dissolved to give a colorless solution. After 90 minutes of stirring at room temperature, a precipitate began to form. The mixture was stirred at 80 ^oC for an additional 2 hours and the solvent was evaporated. The resulting white solids were dissolved in the minimum volume of hot ethanol and the cooled solution was then layered with hexane and stored in the fridge. White solids precipitated from the mixture and were isolated by decanting the supernatant.

Yield: 175 mg (0.33 mmol, 52%).

^1H NMR (d_6-DMSO, 400 MHz), δ_H / ppm: 9.35 (s, 1H, imidazole-2), 8.28 (d, 2H, $^3J_{HH}$ = 8.8 Hz, NO_2-phenyl), 7.85 (s, 1H, imidazole-4 or -5), 7.76 (s, 1H, imidazole-4 or -5), 7.65 (d, 2H, $^3J_{HH}$ = 8.8 Hz, NO_2-phenyl), 7.38 – 7.31 (m, 1.2H, trityl), 7.27 – 7.23 (m, 0.4H, trityl), 5.64 (s, 2H, benzyl). In the imidazolium compound, the trityl group appears to undergo rotation, such that at room temperature, those aromatic protons resonances are very broad and the integration is very small. However, from the mass spectrum, the trityl group is clearly present.

$^{13}C\{^1H\}$ NMR (d_6-DMSO, 100.6 MHz), δ_C / ppm: 147.5 (*ipso*-nitrophenyl), 144.1 (trityl 4^o methyl), 142.4 (*ipso*-nitrophenyl), 136.0 (imidazole-2), 130.6 (trityl *ipso*-phenyl), 129.4 (nitrophenyl C–H), 128.1 (trityl C–H), 127.9 (trityl C–H), 126.9 (trityl C–H), 124.0 (nitrophenyl C–H), 122.2 (imidazole-4 or -5), 120.7 (imidazole-4 or -5), 50.7 (benzyl).

FT-IR (ATR plate), ν / cm^{-1}: 3148 – 2715 (multiple weak bands), 1606 w, 1598 w, 1570 m, 1542 w, 1514 s (nitro N-O stretch), 1494 m, 1438 m, 1342 s (nitro N-O stretch), 1316 m, 1290 m, 1152 m, 1122 w, 1108 w, 1092 w, 1076 m, 1006 w, 864 w, 842 m, 812 w, 798 m, 748 s, 736 s, 698 w, 678 w, 658 w, 624 m, 612 m, 520 w, 476 w.

HRMS (nanochip ESI), *m*/*z*: $[M]^+$ calculated for $C_{29}H_{24}N_3O_2^+$ 446.1869, found 446.1864. Also observed a peak at 204 *m*/*z* that is assigned to $[M - C(C_6H_5)_3]^+$.

NMR Spectra of New Imidazolium Compounds

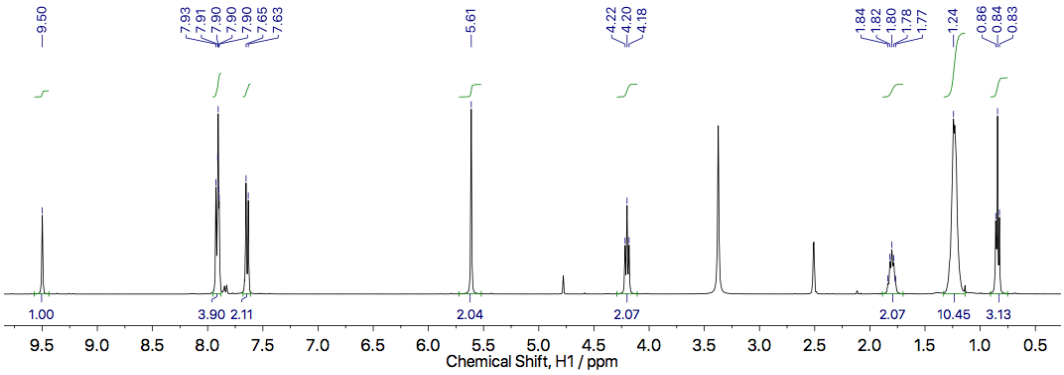

Figure S4. ^{1}H NMR spectrum of **3-CN** in d_6-DMSO.

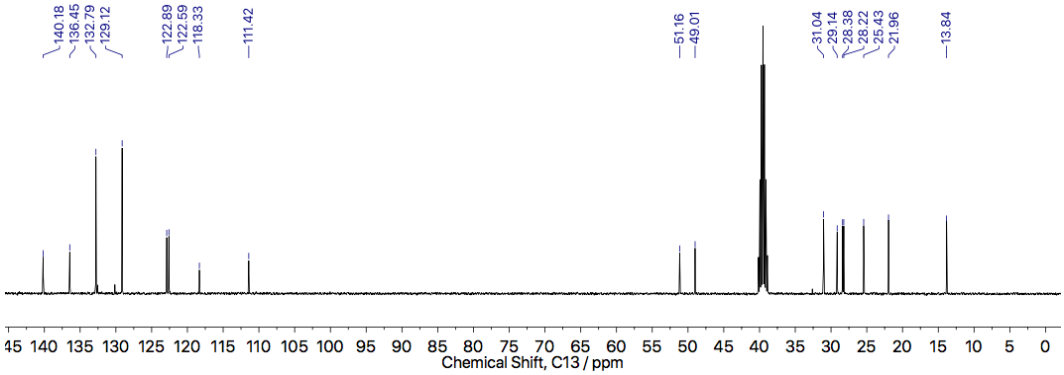

Figure S5. ^{13}C{^{1}H] NMR spectrum of **3-CN** in d_6-DMSO.

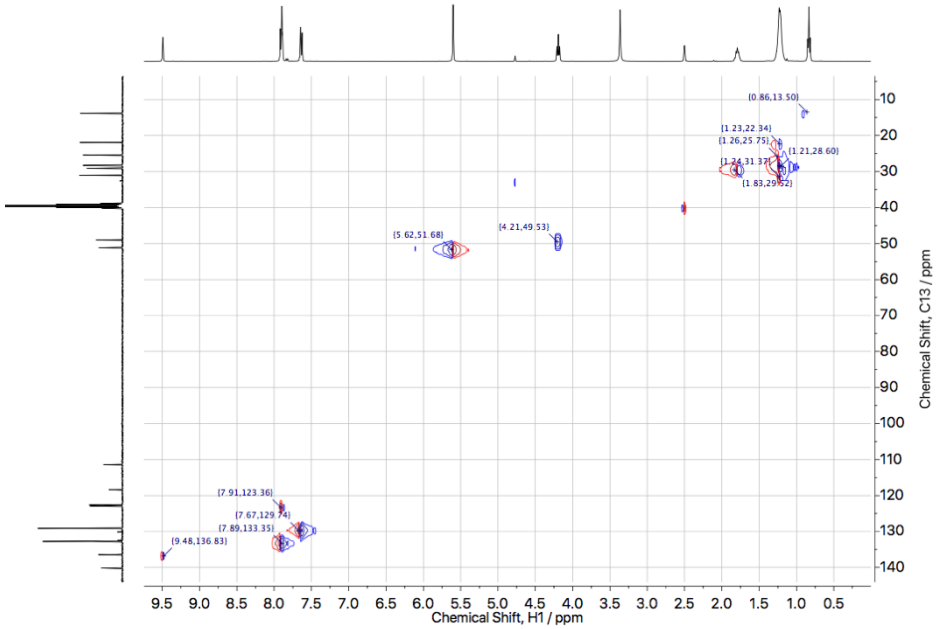

Figure S6. HSQC NMR spectrum of **3-CN** in d_6-DMSO.

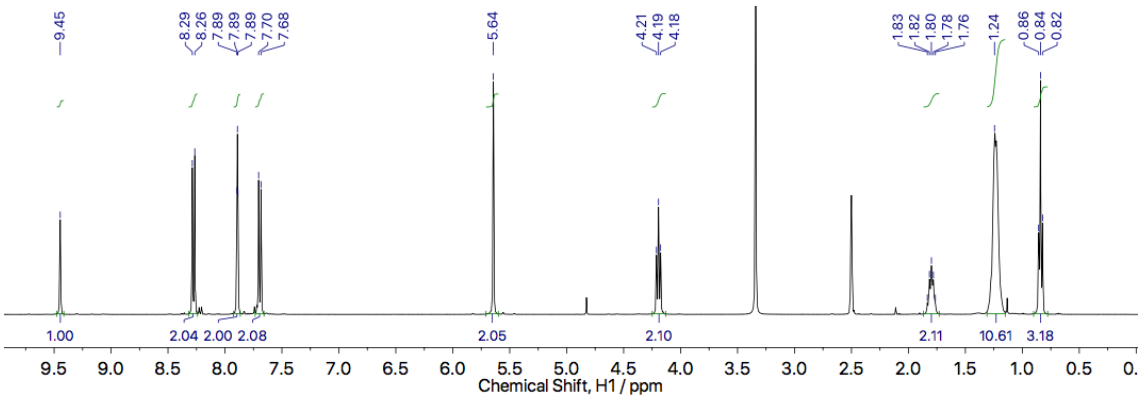

Figure S7. ^{1}H NMR spectrum of **3-NO$_2$** in d_6-DMSO.

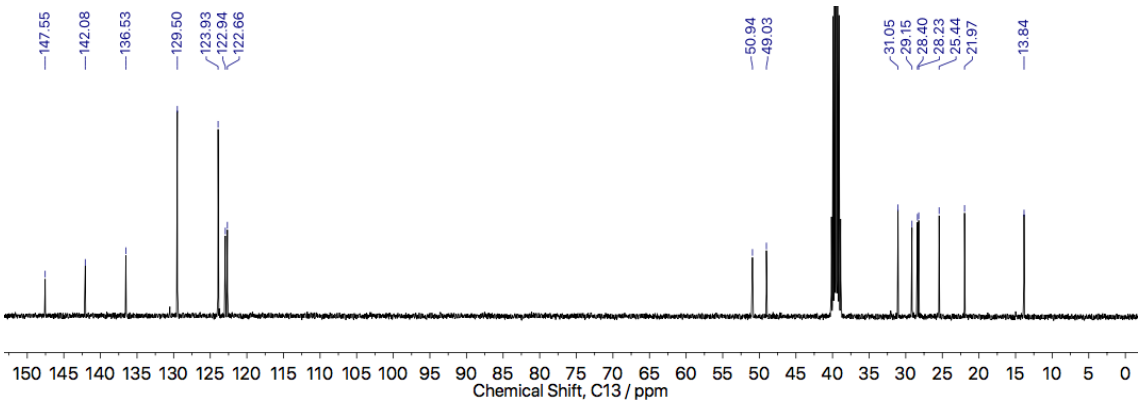

Figure S8. ^{13}C{^{1}H] NMR spectrum of **3-NO$_2$** in d_6-DMSO.

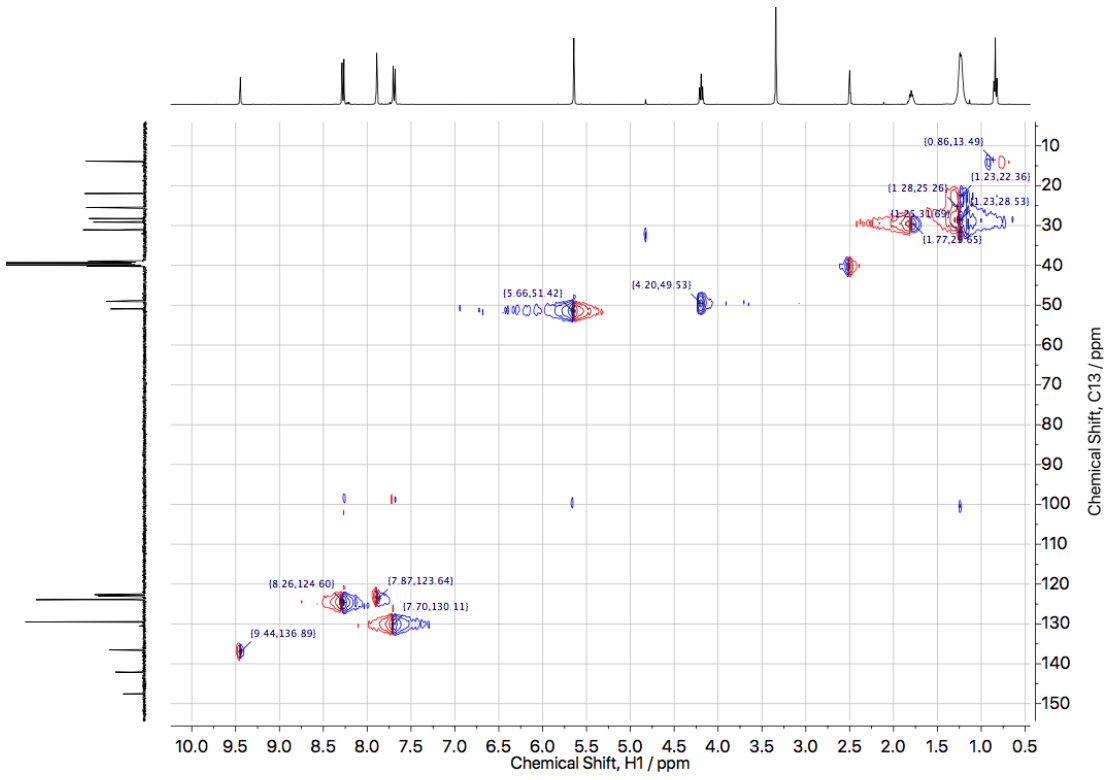

Figure S9. HSQC NMR spectrum of **3-NO$_2$** in d_6-DMSO.

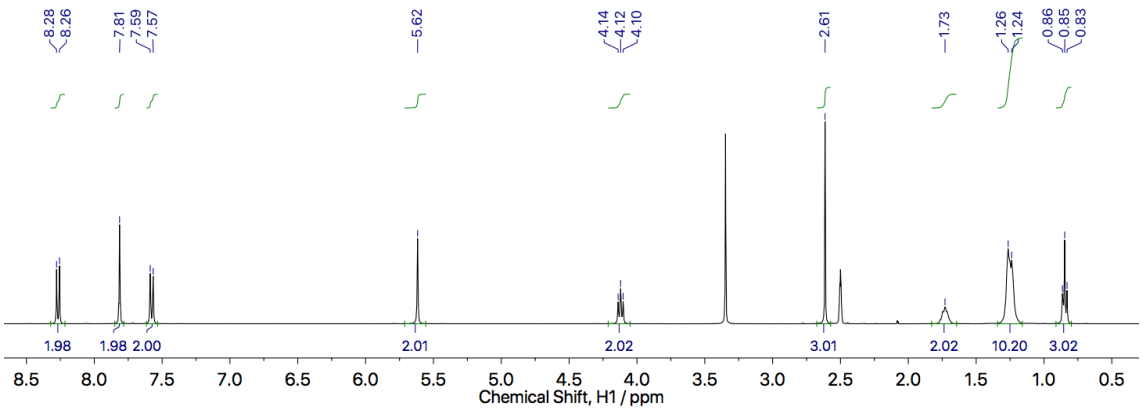

Figure S10. ^{1}H NMR spectrum of **3b-NO$_2$** in d_6-DMSO.

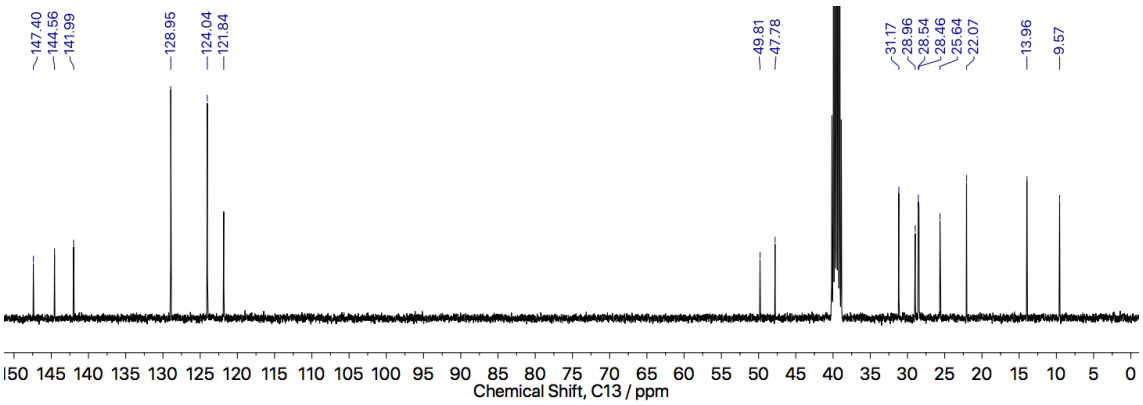

Figure S11. ^{13}C{^{1}H] NMR spectrum of **3b-NO$_2$** in d_6-DMSO.

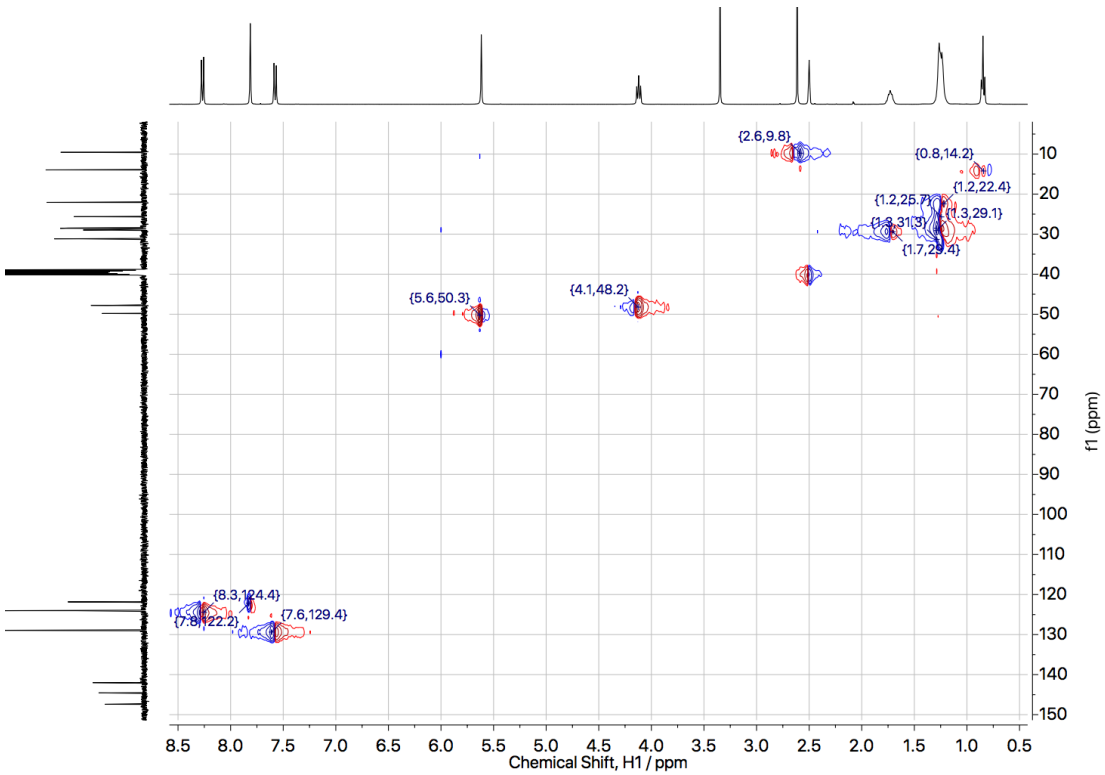

Figure S12. HSQC NMR spectrum of **3b-NO$_2$** in d_6-DMSO.

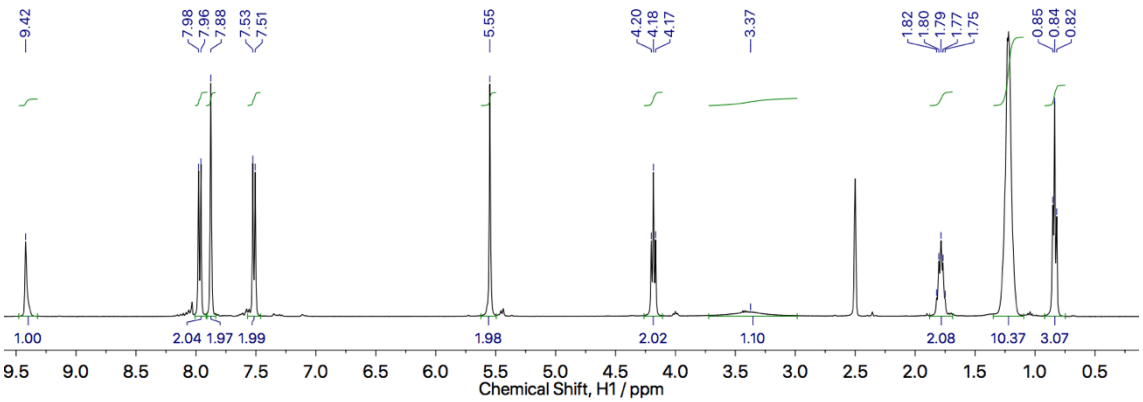

Figure S13. ^{1}H NMR spectrum of **3-CO_2H** in d_6-DMSO.

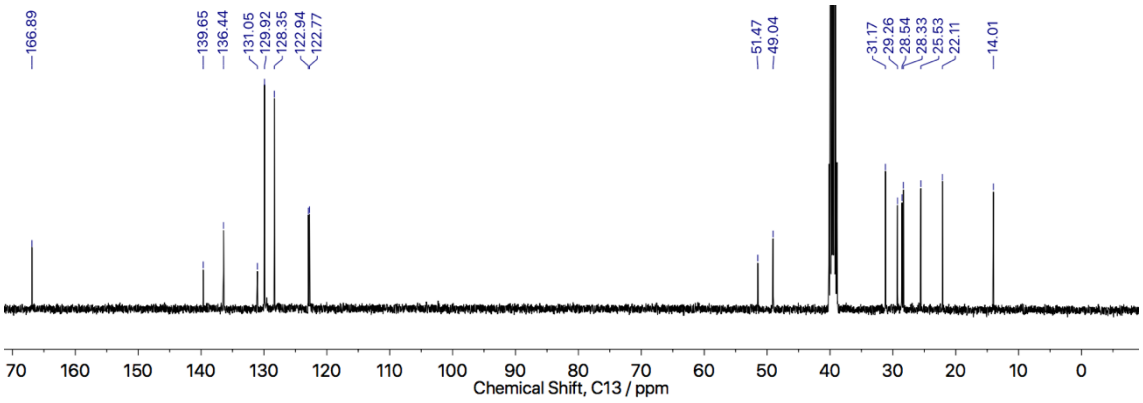

Figure S14. ^{13}C{^{1}H] NMR spectrum of **3-CO_2H** in d_6-DMSO.

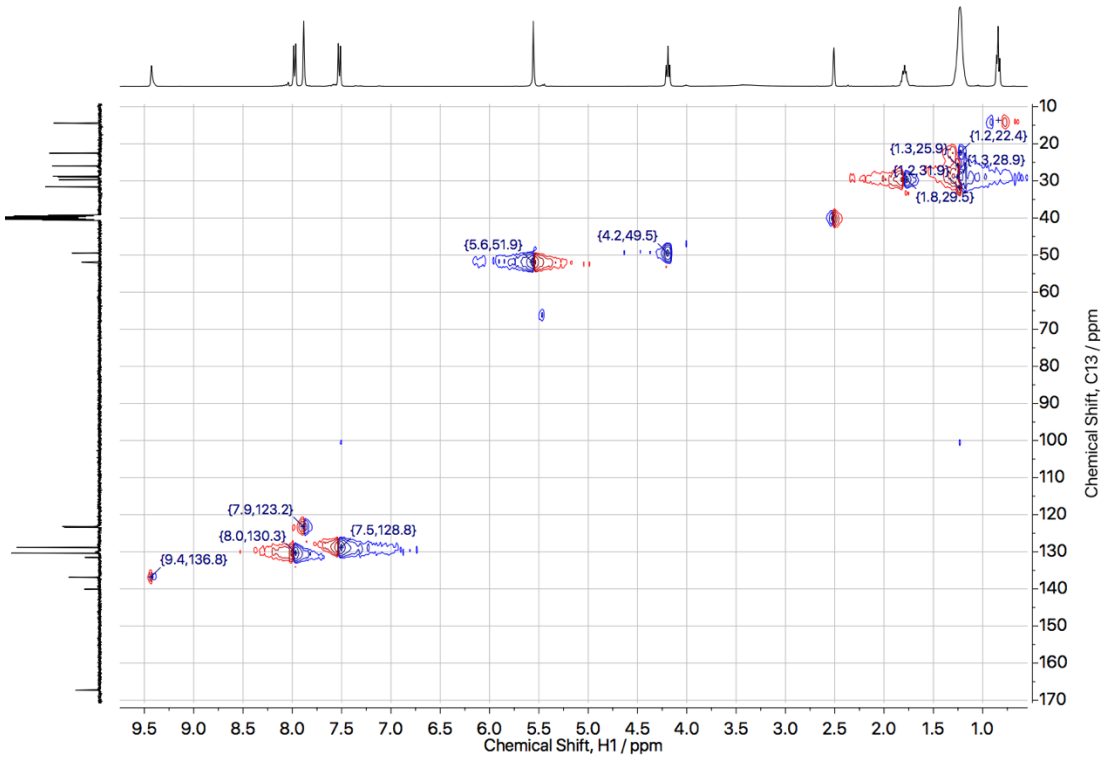

Figure S15. HSQC NMR spectrum of **3-CO_2H** in d_6-DMSO.

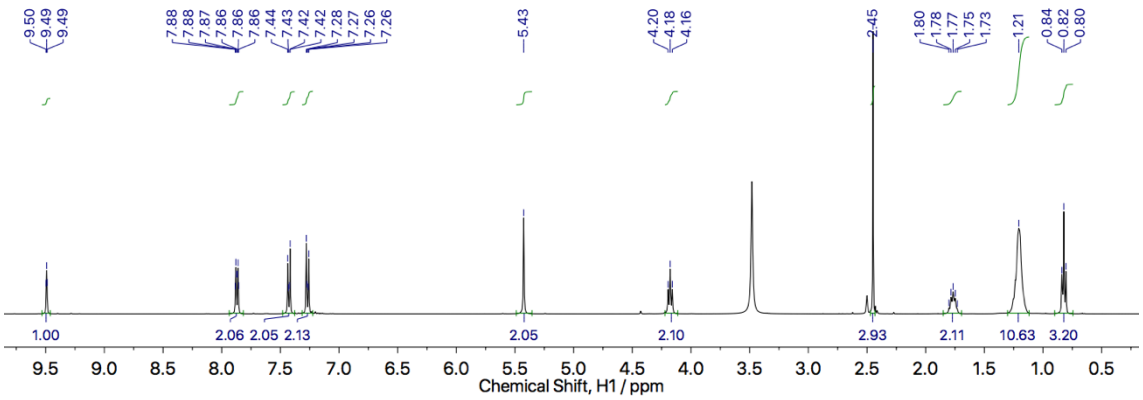

Figure S16. ^{1}H NMR spectrum of **3-SCH$_3$** in d_6-DMSO.

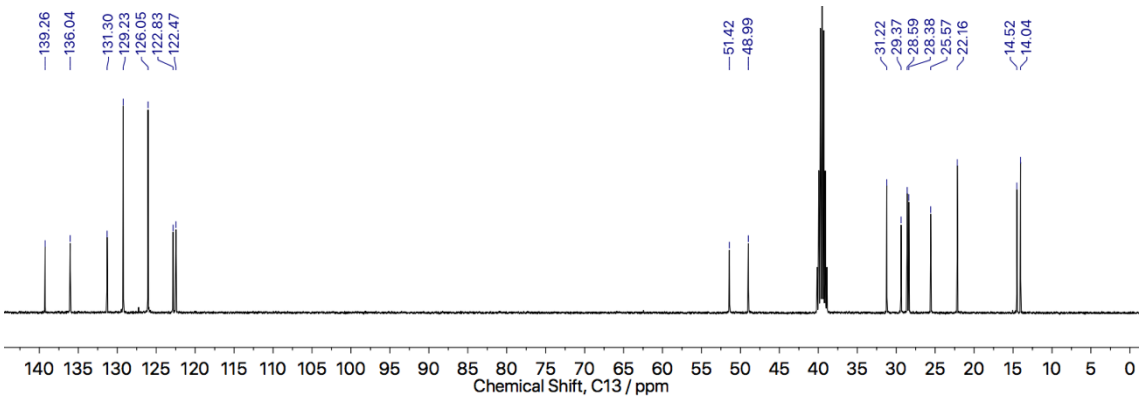

Figure S17. ^{13}C{^{1}H] NMR spectrum of **3-SCH$_3$** in d_6-DMSO.

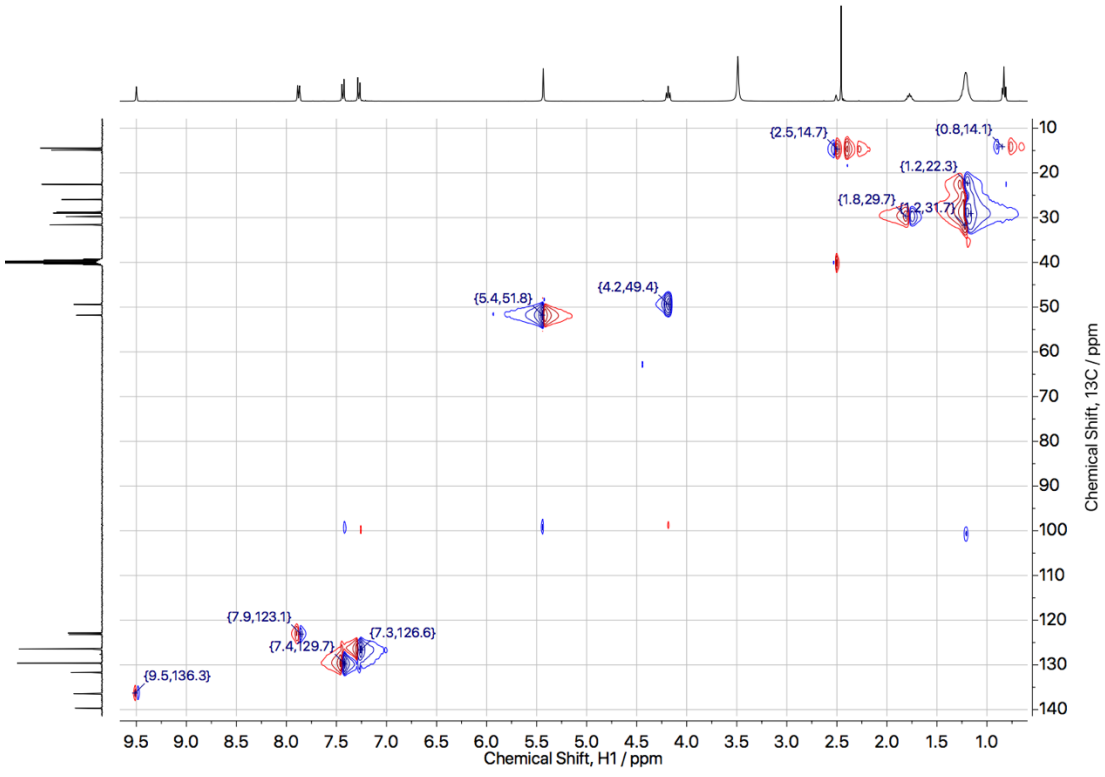

Figure S18. HSQC NMR spectrum of **3-SCH$_3$** in d_6-DMSO.

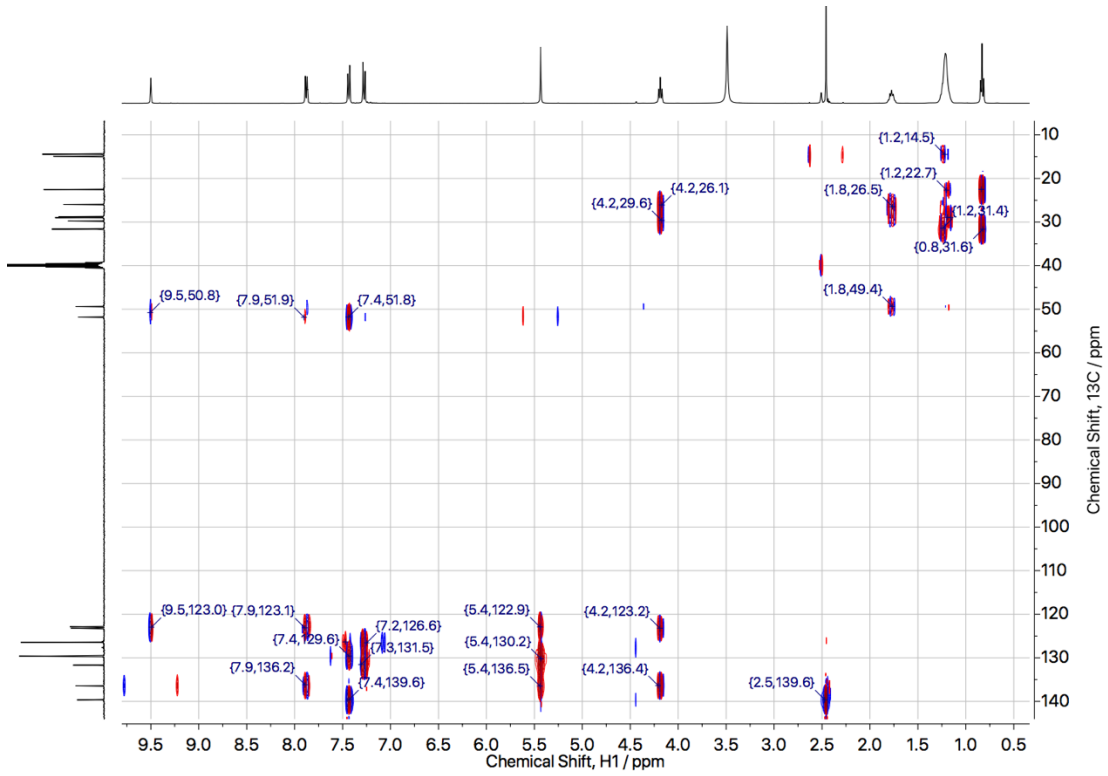

Figure S19. HMBC NMR spectrum of **3-SCH$_3$** in d_6-DMSO.

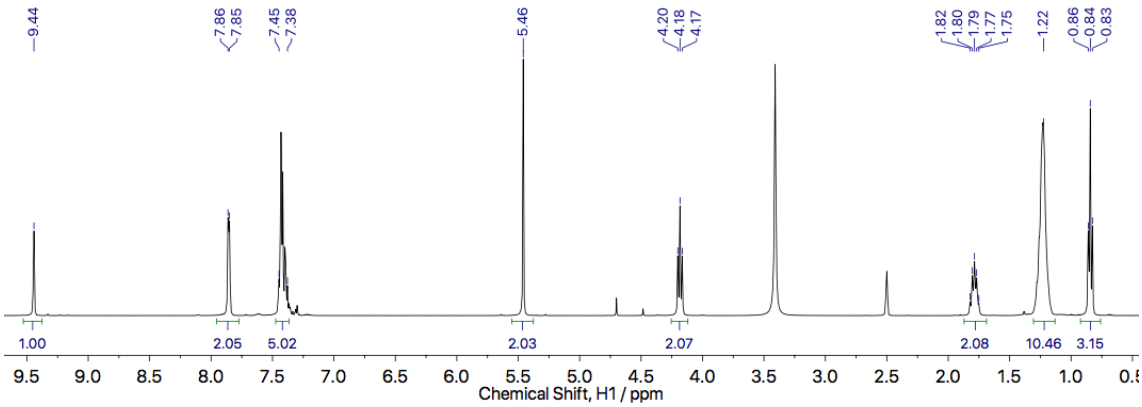

Figure S20. ^{1}H NMR spectrum of **3-H** in d_6-DMSO.

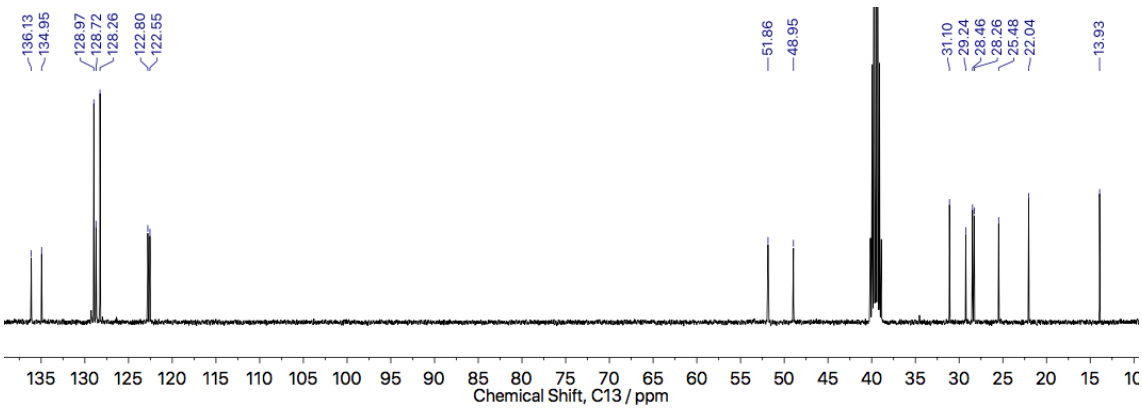

Figure S21. ^{13}C{^{1}H} NMR spectrum of **3-H** in d_6-DMSO.

Figure S22. HSQC NMR spectrum of **3-H** in d_6-DMSO.

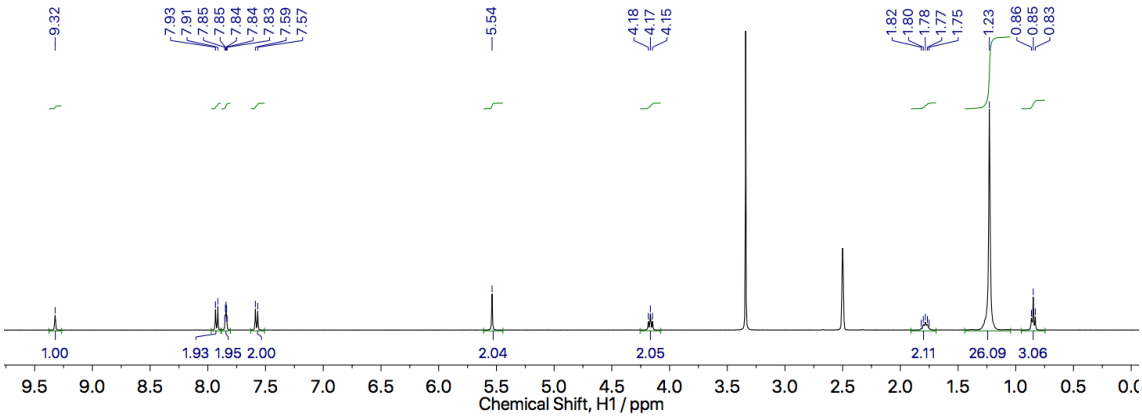

Figure S23. ^{1}H NMR spectrum of **4-CN** in d_6-DMSO.

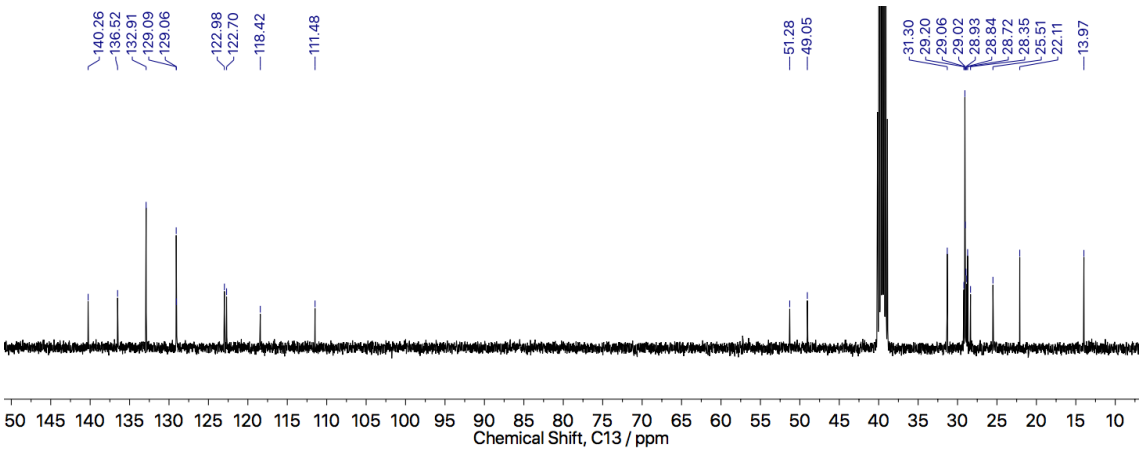

Figure S24. ^{13}C{^{1}H} NMR spectrum of **4-CN** in d_6-DMSO.

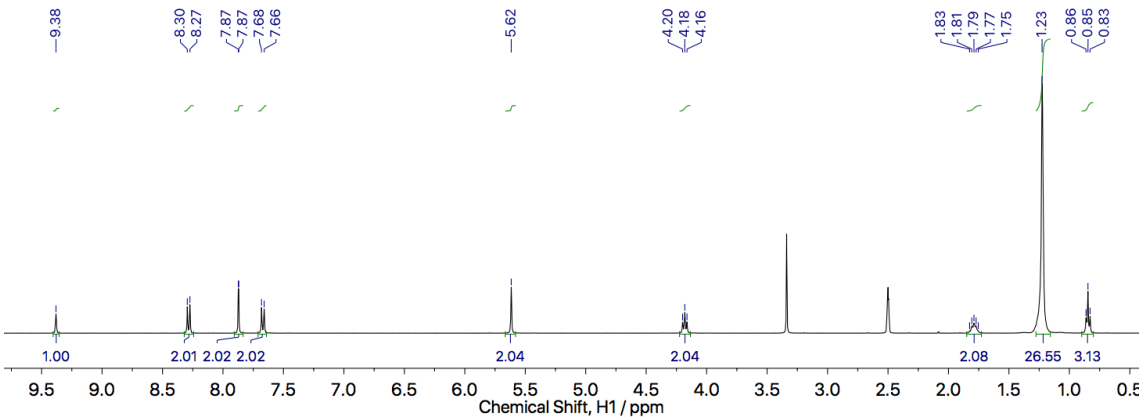

Figure S25. ^{1}H NMR spectrum of **4-NO$_2$** in d_6-DMSO.

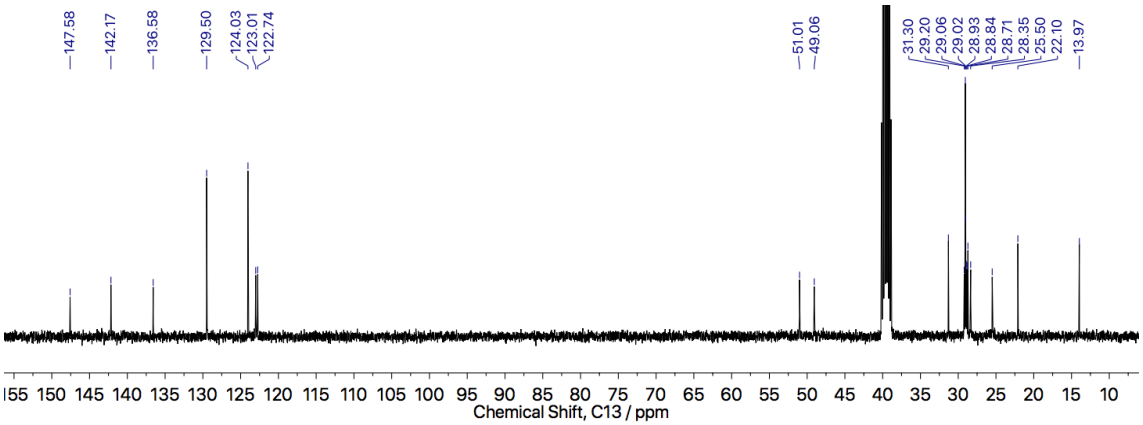

Figure S26. ^{13}C{^{1}H} NMR spectrum of **4-NO$_2$** in d_6-DMSO.

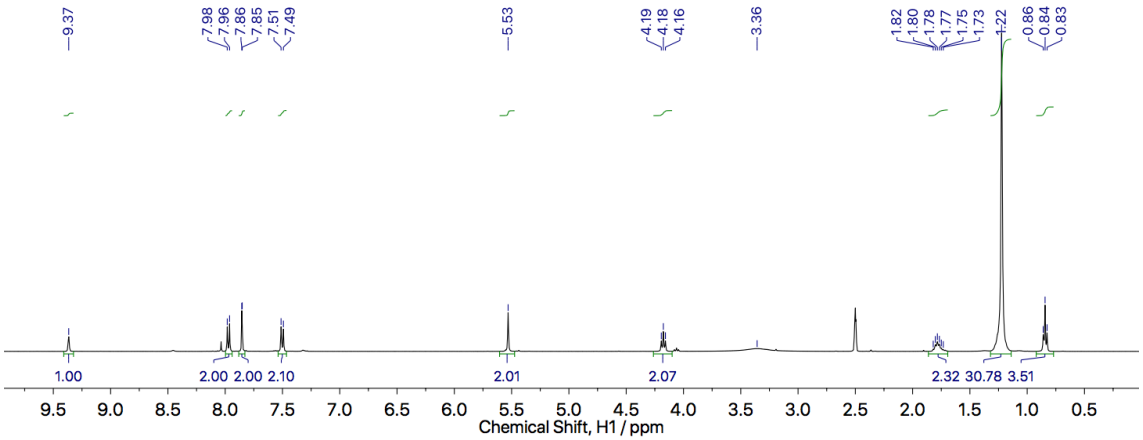

Figure S27. ^{1}H NMR spectrum of **4-CO$_2$H** in d_6-DMSO.

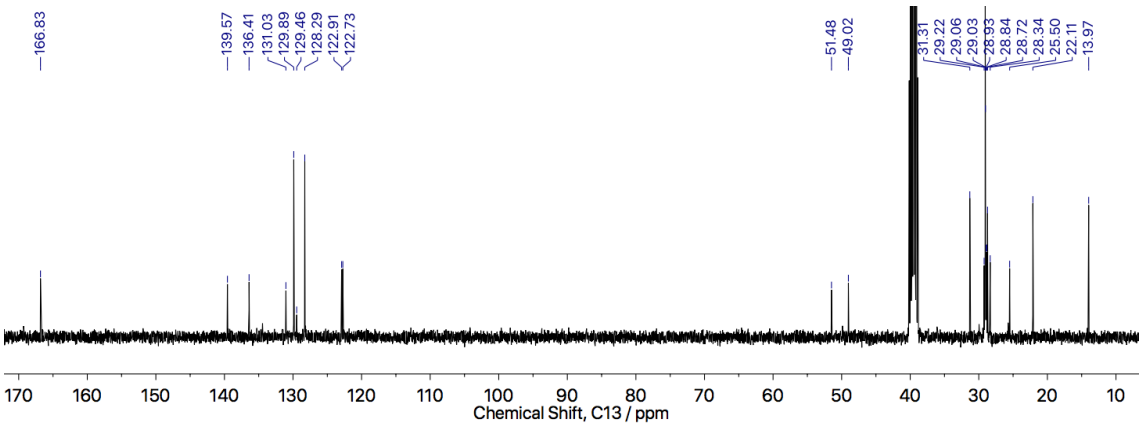

Figure S28. $^{13}C\{^{1}H\}$ NMR spectrum of **4-CO_2H** in d_6-DMSO.

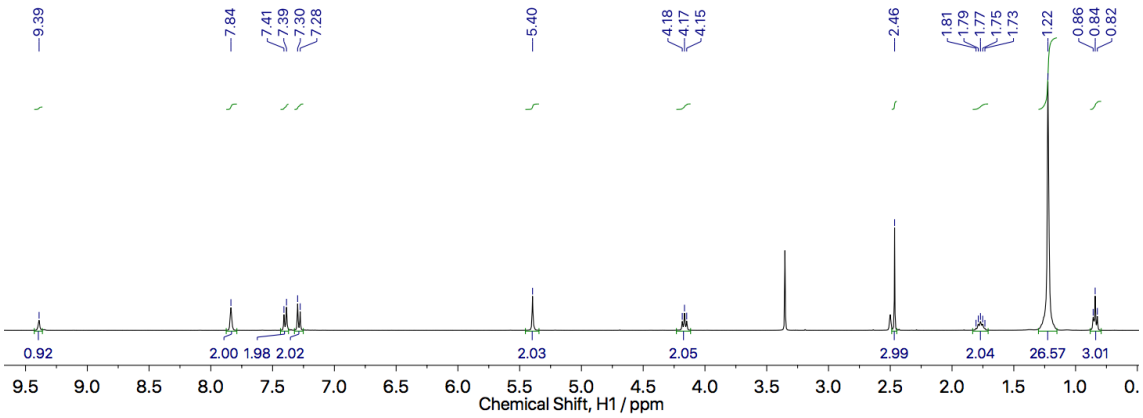

Figure S29. ^{1}H NMR spectrum of **4-SCH_3** in d_6-DMSO.

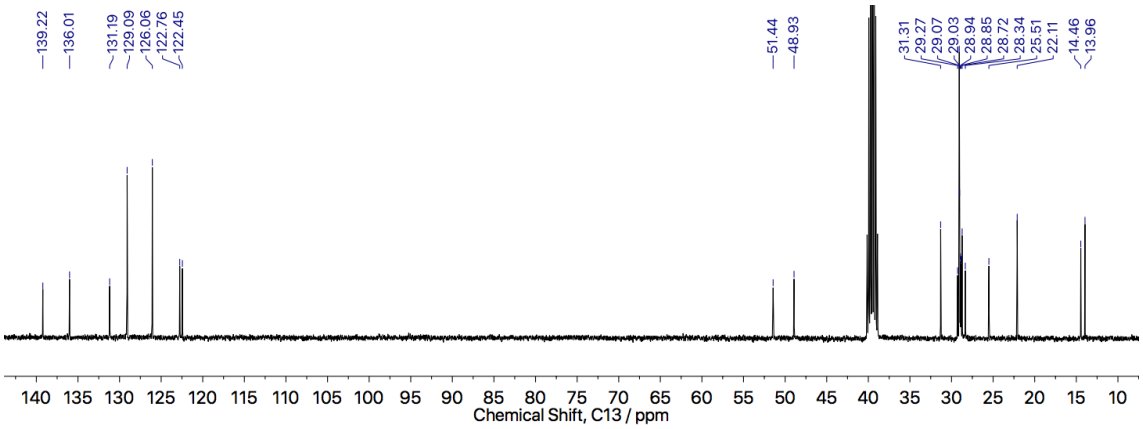

Figure S30. $^{13}C\{^{1}H\}$ NMR spectrum of **4-SCH_3** in d_6-DMSO.

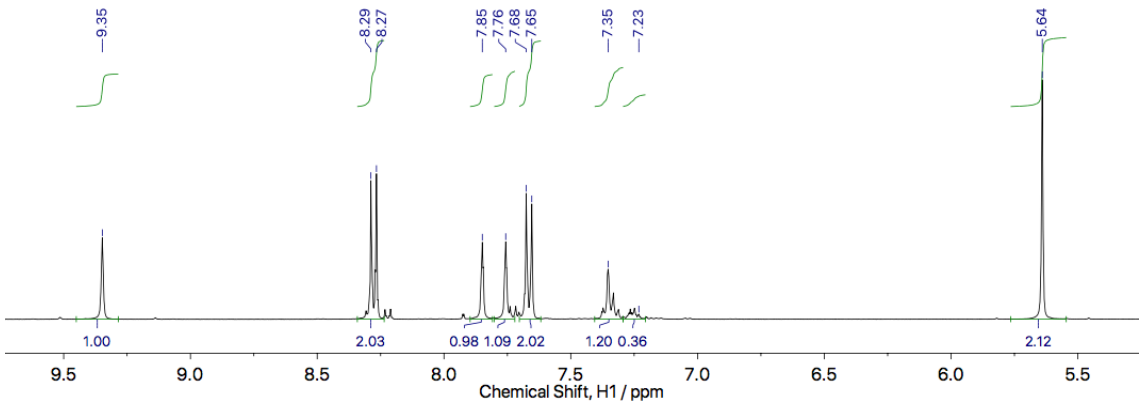

Figure S31. ^{1}H NMR spectrum of **5-NO$_2$** in d_6-DMSO.

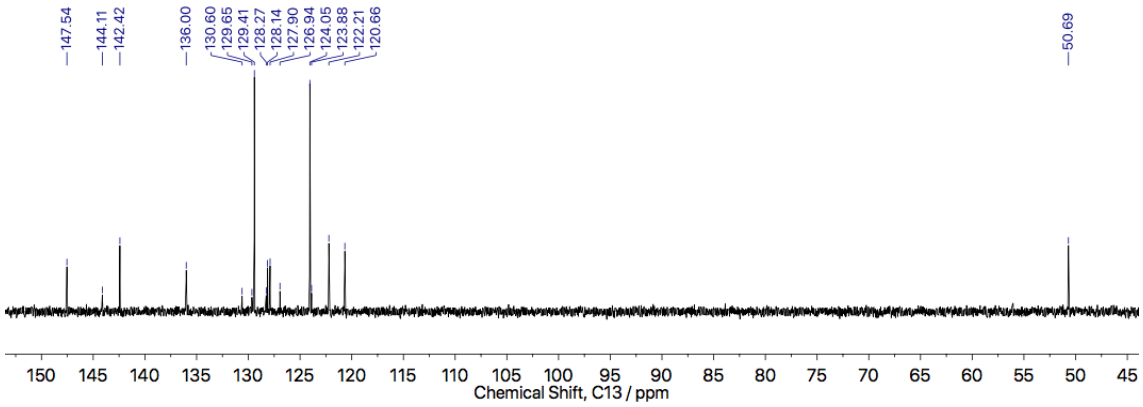

Figure S32. ^{13}C{^{1}H} NMR spectrum of **5-NO$_2$** in d_6-DMSO.

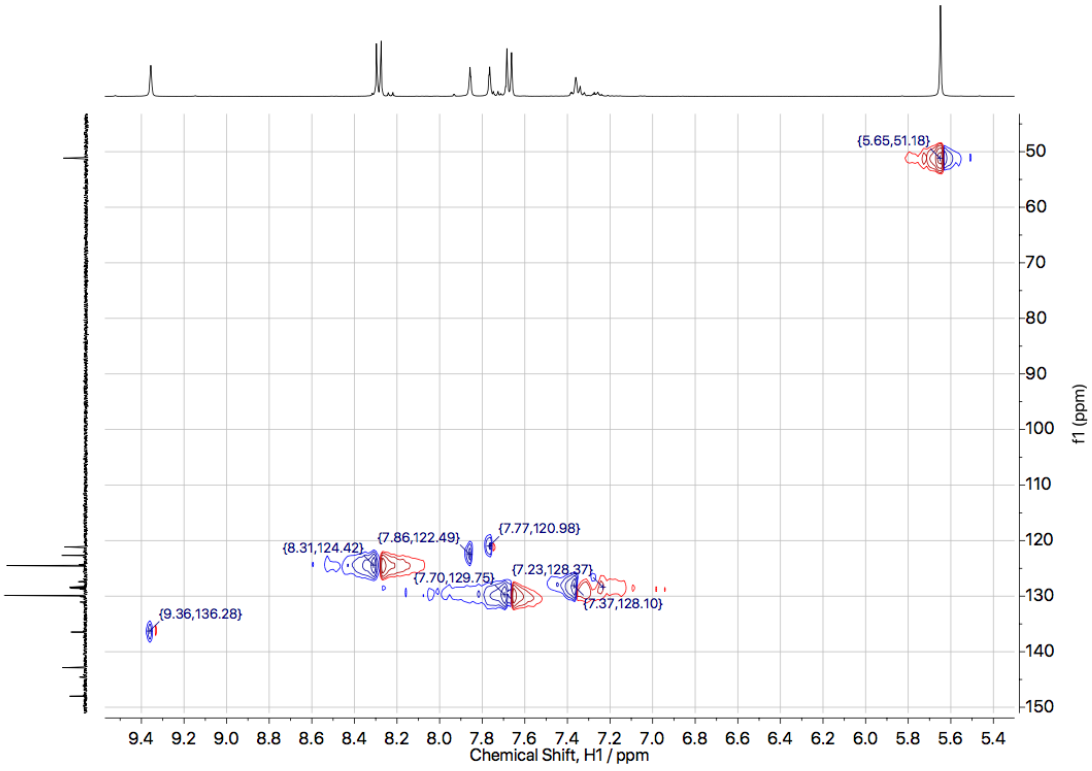

Figure S33. HSQC NMR spectrum of **5-NO$_2$** in d_6-DMSO.

TEM images and discussion on developing the ligand exchange procedure

Ligand exchange was initially carried out directly in solution, typically suspending 12 nm AgNCs in hexane, or mixtures of hexane/ethanol or hexane/acetone. In all cases, sintering of the nanocrystals to form large metallic blocks (*ca*. 150 nm) was observed. This occurred when:

- Washing the AgNCs with hexane/acetone to remove the native OLAM ligands;
- Adding an excess of the new imidazolium ligands (in ethanol) directly to stable suspensions of Ag-OLAM (in hexane). See Figure S34. This occurred regardless of concentration or solvent polarity.
- Stripping native OLAM ligands from AgNCs using Meerwein's salt, and adding the new imidazolium ligands (see Figure S35).

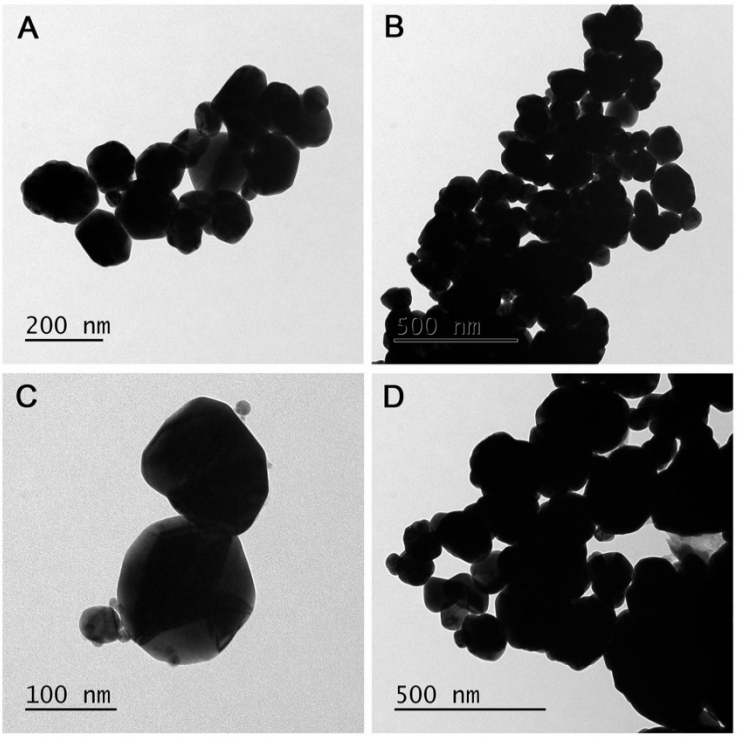

Figure S34. TEM images of AgNCs following ligand exchange with **(a) 3-NO_2 (b) 3-CN (c) 3-CO_2H** and **(d) 3-SCH_3**. Ligand exchange was carried out in solution, adding the new ligands (in ethanol) to a suspension of OLAM-bearing AgNCs in hexane.

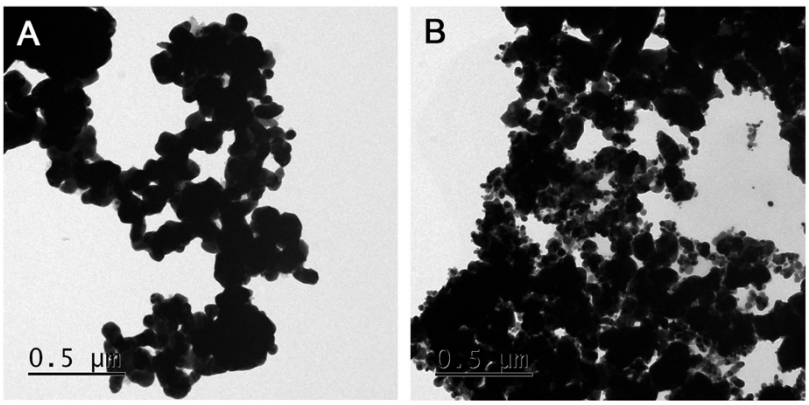

Figure S35. TEM images of AgNCs following ligand exchange with **(a) 3-NO_2 (b) 4-NO_2**. Ligand exchange was carried out by first stripping OLAM ligands from AgNCs using Meerwein's Salt, $[Me_3O][BF_4]$, in acetonitrile, and then adding the new ligands as solutions in ethanol/hexane.

Additional notes on the ligand exchange procedure discussed in the main text:

- Sintering was observed when pure acetone was used for the ligand exchange procedure described in the main text (Figure S36A).
- An excess of ligands was always used, working under the assumption that the AgNCs would always be saturated with the maximum number of ligands during the ligand exchange.
- For the recovery of hybrid AgNCs from the substrates, the substrates were immersed in DMSO, where the hybrid AgNCs rapidly formed suspensions. Recovery was unsuccessful using ethanol, chloroform, water or acetonitrile. After recovery in DMSO, the suspensions could be diluted in methanol, ethanol, iso-propanol, water, 0.1 M $KHCO_{3\,(aq)}$ or acetonitrile, forming yellow suspensions.

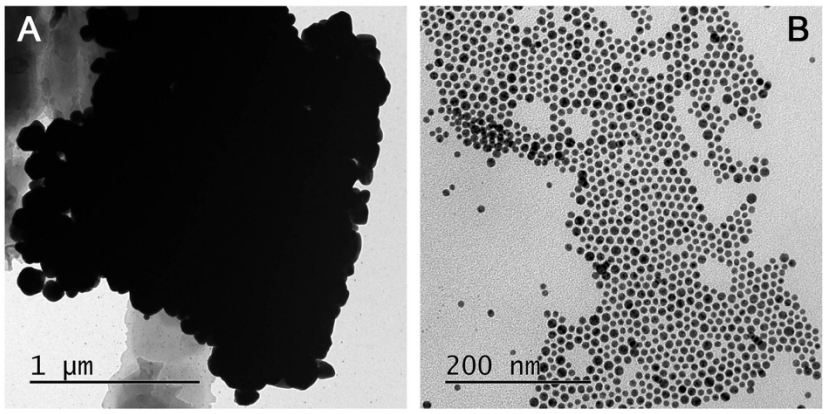

Figure S36. TEM images of AgNCs following ligand exchange with **3-CN**. OLAM-bearing AgNCs were first drop-cast onto Si-wafer substrates and then immersed in ligand solutions of **(a)** acetone and **(b)** 1:1 hexane/acetone.

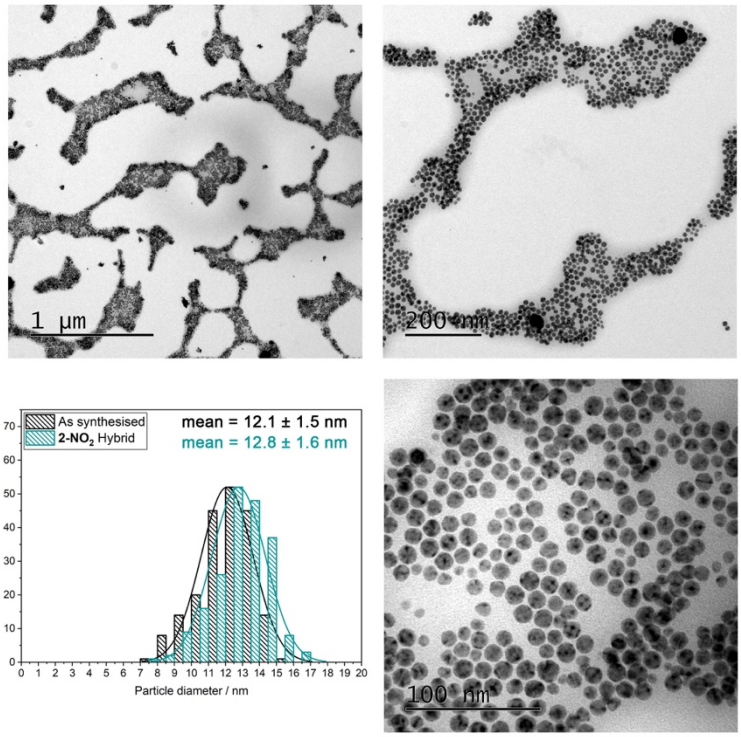

Figure S37. TEM images of AgNCs following ligand exchange with **2-NO_2**. AgNCs were deposited on TEM grids, immersed in a 1:1 hexane/ethanol solution of **2-NO_2** for 5 minutes and then dipped three times in clean ethanol. The size distribution of the hybrid AgNCs is also shown as a histogram, along with that for the as-synthesised NCs for comparison.

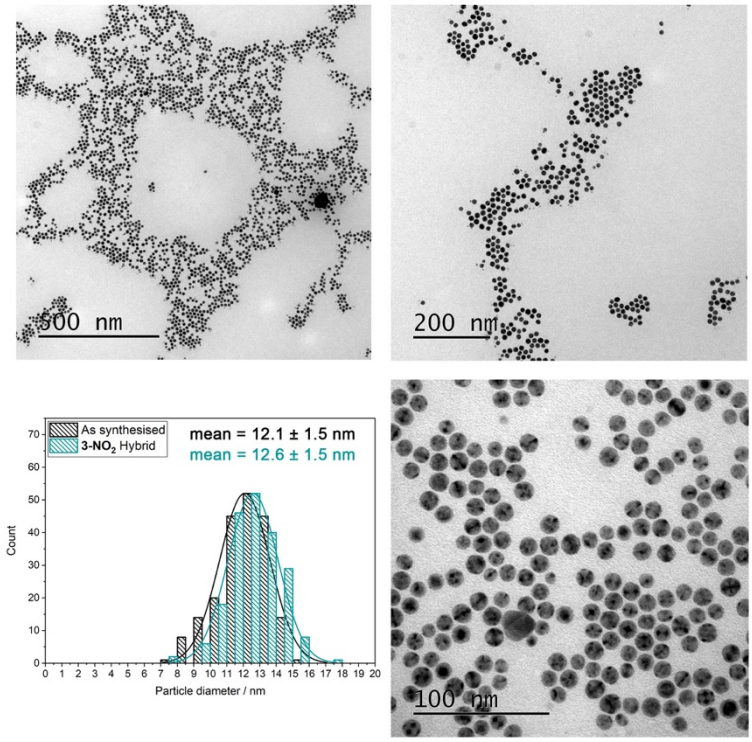

Figure S38. TEM images of AgNCs following ligand exchange with **3-NO_2**. AgNCs were deposited on TEM grids, immersed in a 1:1 hexane/ethanol solution of **3-NO_2** for 5 minutes and then dipped three times in clean ethanol. The size distribution of the hybrid AgNCs is also shown as a histogram, along with that for the as-synthesised NCs for comparison.

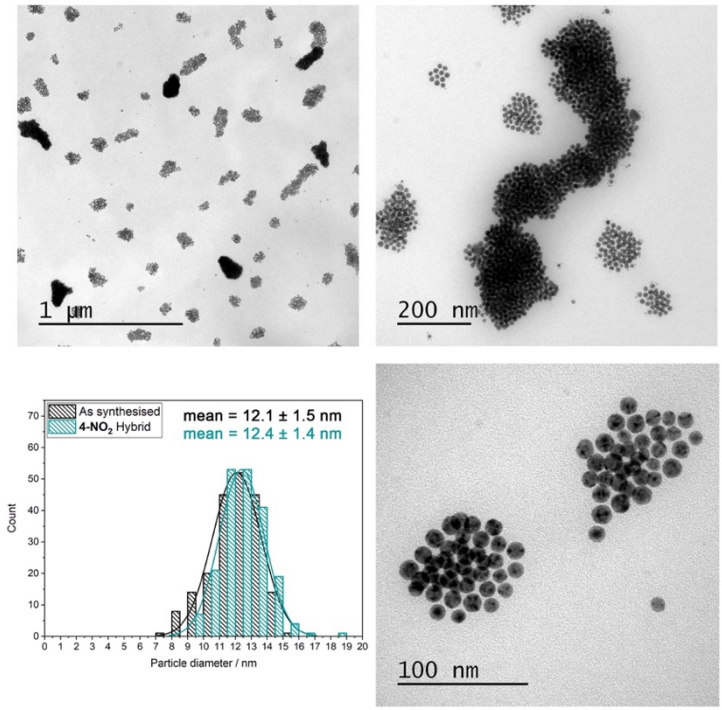

Figure S39. TEM images of AgNCs following ligand exchange with **4-NO_2**. AgNCs were deposited on TEM grids, immersed in a 1:1 hexane/ethanol solution of **4-NO_2** for 5 minutes and then dipped three times in clean ethanol. The size distribution of the hybrid AgNCs is also shown as a histogram, along with that for the as-synthesised NCs for comparison.

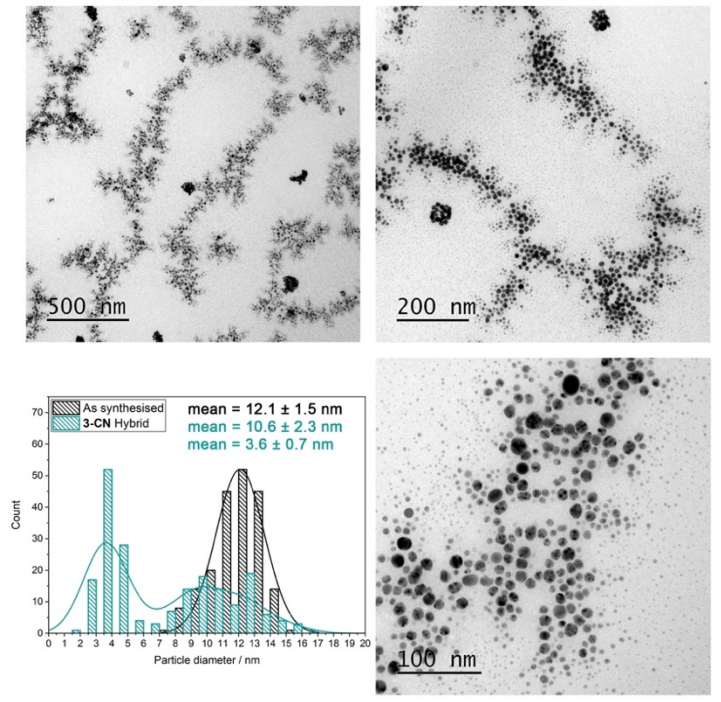

Figure S40. TEM images of AgNCs following ligand exchange with **3-CN**. AgNCs were deposited on TEM grids, immersed in a 1:1 hexane/ethanol solution of **3-CN** for 5 minutes and then dipped three times in clean ethanol. The size distribution of the hybrid AgNCs is also shown as a histogram, along with that for the as-synthesised NCs for comparison. The size distribution histogram for **3-CN** is based on measurements of 100 large particles and 100 small particles; the histogram does not accurately represent the ratio between large and small particles.

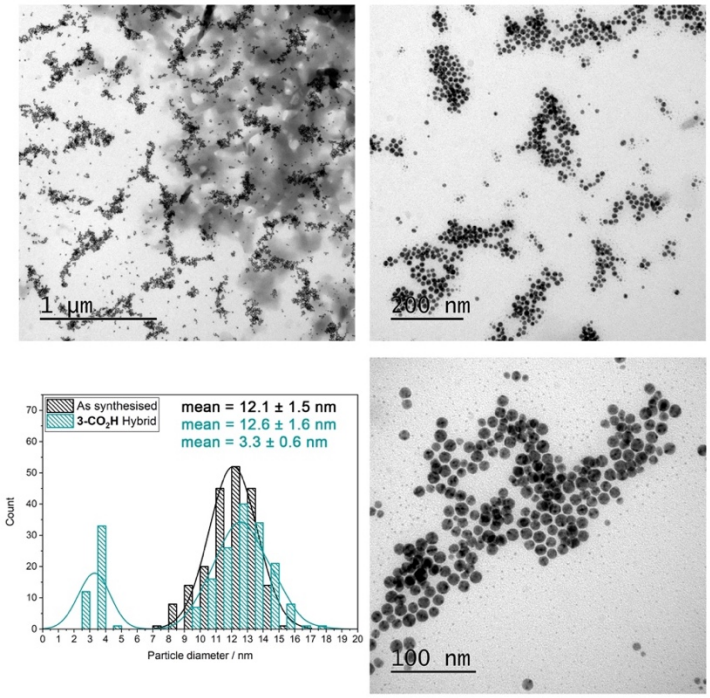

Figure S41. TEM images of AgNCs following ligand exchange with **3-CO_2H**. AgNCs were deposited on TEM grids, immersed in a 1:1 hexane/ethanol solution of **3-CO_2H** for 5 minutes and then dipped three times in clean ethanol. The size distribution of the hybrid AgNCs is also shown as a histogram, along with that for the as-synthesised NCs for comparison. The size distribution histogram for **3-CO_2H** is based on measurements of 150 large particles and 50 small particles; the histogram does not accurately represent the ratio between large and small particles.

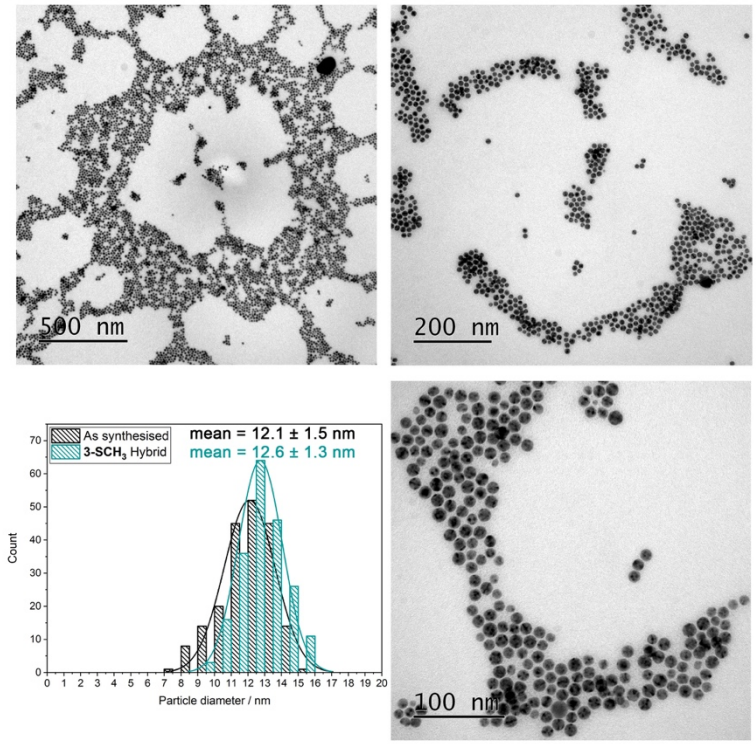

Figure S42. TEM images of AgNCs following ligand exchange with **3-SCH_3**. AgNCs were deposited on TEM grids, immersed in a 1:1 hexane/ethanol solution of **3-SCH_3** for 5 minutes and then dipped three times in clean ethanol. The size distribution of the hybrid AgNCs is also shown as a histogram, along with that for the as-synthesised NCs for comparison.

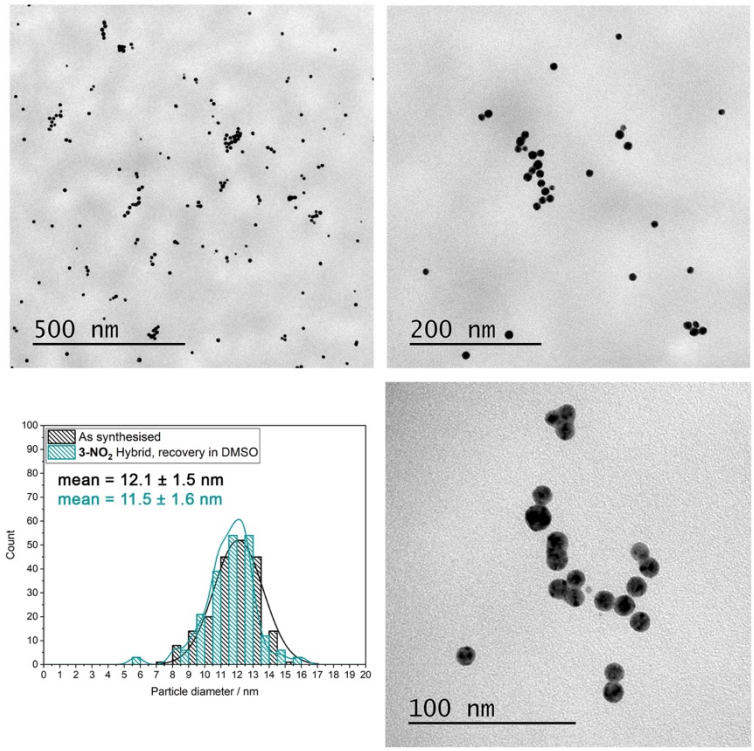

Figure S43. TEM images of AgNCs following ligand exchange with **3-NO_2**. AgNCs were deposited on p-doped Si, immersed in a 1:1 hexane/ethanol solution of **3-NO_2** for 5 minutes and then dipped three times in clean ethanol. After drying, the hybrid AgNCs were recovered in DMSO and then drop-cast onto a TEM grid for imaging. The size distribution of the hybrid AgNCs is also shown as a histogram, along with that for the as-synthesised NCs for comparison.

^{1}H NMR Spectra of Hybrid AgNCs

The hybrid AgNCs (i.e. ligand functionalized Ag NCs) were characterised by ^{1}H NMR spectroscopy after redispersion in d_6-DMSO from Si substrates. Compared with the free ligands, the hybrid AgNC samples displayed resonances at lower chemical shift, which implies that the ligands are more electron rich when bound to the Ag surface, which is in agreement with the XPS data (below). Our main aim of measuring the NMR spectra for our catalysts was to verify that the ligands were present on the surface. However, we also discovered some interesting details in the NMR spectra, that we believe are related to the ligand arrangement at the surface. Here, we provide a discussion that seeks to make some tentative conclusions to explain these NMR data.

For nearly all the hybrid samples, two sets of ligand resonances were observed: the first was only slightly shifted in comparison with the free ligand (*ca*. 0.2 ppm for Im-2H); the other was shifted much more significantly (*ca*. 1 ppm for Im-2H, Figure S44). We suspected that two different orientations of the ligands on the surface were responsible for these two sets of resonances. This hypothesis is supported by a related case in the literature, where aromatic thiol ligands on Au were found to adopt a 'lying down' arrangement at low ligand concentrations (binding to the metal through electrostatic interactions); with higher ligand concentrations, the ligands rearranged into a 'standing up' mode so as to facilitate closer packing of ligands on the surface.[8] Given that our ligands are similarly made of aromatic groups and include ligating donor atoms, we reason that our ligands can also be found in a 'lying down' mode (referred to here as a parallel mode, $\parallel$, see Figure S44) or a 'standing up' mode (referred to here as a perpendicular mode, $\perp$).

In order to further investigate this mixture of ligand arrangements on the surface, we prepared a series of **Ag-3-NO$_2$** samples using increasing ligand concentrations in the exchange ([L]). In the resulting ^{1}H NMR spectra (Figure S45), there were indeed clear dependencies of the ligand resonances on the ligand concentration. When [L] was 1.4 mM or less, only the set of resonances at high chemical shift were observed. When [L] was between 1.4 mM and 7.0 mM, a second set of phenyl doublets could be observed. When [L] was much higher still (above 22.2 mM), a second Im-2H resonance could also be observed. Thus, the data suggest that the imidazolium ligands arrange themselves in a concentration-dependent fashion. In agreement with the related case in the literature,[8] we can therefore infer the set of resonances at higher chemical shift appearing at lower ligand concentration to the parallel mode, and the ones at the higher ligand concentrations (as used in the catalyst preparation) to the perpendicular mode.

The assignment of the parallel mode to the resonances at higher chemical shift and of the perpendicular mode to the resonances at lower chemical shift is also in agreement with an additional study from the literature.[9] Using TOCSY (total correlated spectroscopy) NMR, the authors were able to fully assign different ligand arrangements (again, aromatic thiols) on the Au surface. They found that ligand-to-metal interactions moved the ligand resonances to higher chemical shift, and that various ligand-to-ligand interactions moved the ligand resonances to lower chemical shift. In our case, the parallel mode will maximise ligand-to-metal interactions, as the aromatic groups are lying directly against the surface – we therefore expect this mode to appear at higher chemical shift. Conversely, in the perpendicular mode, each ligand is standing up and is surrounded by other ligands; as such, we expect this mode to appear at lower chemical shift.

The mixture of binding modes was also observed for **3-H**, which does not feature a ligating atom in the anchor group (Figure S51). However, despite the lack of an anchoring group that can form covalent/dative bonds with the surface, we argue that it is the concentration of ligands at the surface that enforces the perpendicular binding mode for this ligand, akin to a self-assembled monolayer. The hypothesis of the presence of the parallel/perpendicular binding modes is further supported when we look at the spectrum for **5-NO_2** (Figure S52). This was the only hybrid sample that displayed a single ligand arrangement, with the resonances being found in the region expected for the perpendicular mode. Here, the bulky trityl group will block the parallel binding mode

Finally, we carried out ^{1}H-^{1}H nuclear Overhauser effect NMR spectroscopy (NOESY) to confirm that the ligand resonances observed were due to surface-bound ligands. For the 2D NOESY spectrum of the free ligand, **3-NO_2**, the cross peaks indicate that NOE interactions are only present between neighbouring ^{1}H nuclei within *ca*. 3 Å, as is typical (Figure S53). Furthermore, the cross peaks are positive (that is to say, of opposite sign to the diagonal peaks), indicating that the double-quantum cross-relaxation pathway is dominant.[10] In contrast, for **Ag-3-NO_2**, intense and *negative* cross peaks were observed (cross and diagonal peaks are of the same sign), showing that the zero-quantum cross-relaxation pathway is dominant in this case (Figure S54). This is to be expected for slowly tumbling species (such as organic ligands bound to a large NC), where the rotational correlation time, $\tau_c << 1/\omega_0$, where ω_0 is the angular frequency of the spectrometer.[11] In addition, NOE interactions were observed between ^{1}H environments that are well beyond 3 Å, which is a phenomenon observed for molecules on NC surfaces.[10] Importantly, both parallel and perpendicular sets of resonances were confirmed as arising from surface-bound ligands.

Finally, we highlight that from the NMR data alone, we are unable to discern explicitly that the anchor functional groups (i.e. CN, NO_2, CO_2H, SCH_3) are pointing directly at the surface and that strong covalent interactions result. However, regardless of the specific orientation of the ligands, there is clearly a strong influence of the different anchor groups on the Ag electronic structure and the catalysis (XPS, Figures 4 and S64). If the anchor groups were not interacting with the surface at all, we would not expect such observations.

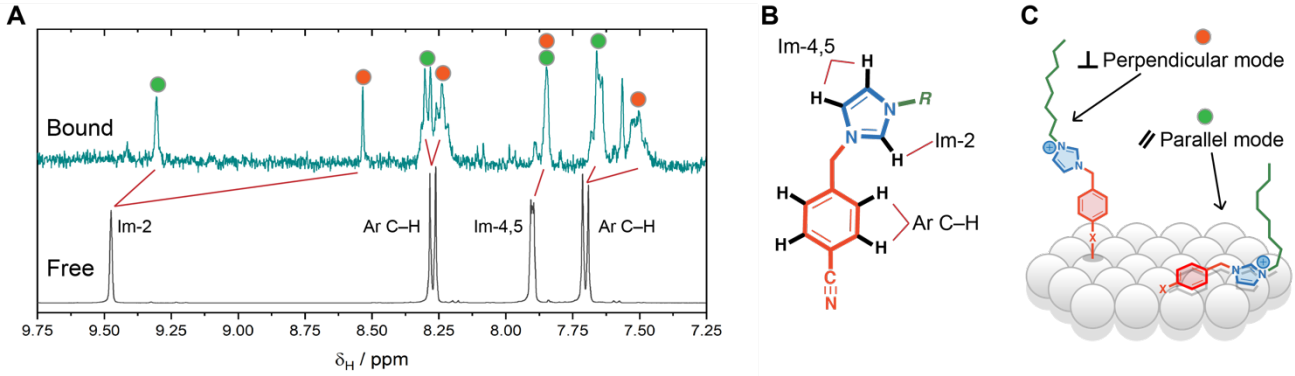

Figure S44. A) ^{1}H NMR spectra of **3-NO$_2$** and **Ag-3-NO$_2$**, showing assignments of the aromatic proton resonances for the ligand (shown schematically in (**B**). Green spots indicate the ligand resonances that are observed at low ligand concentrations, which are assigned to a parallel binding mode (as in **C**). Orange spots indicate the ligand resonances that are observed at high ligand concentrations, which are assigned to a perpendicular binding mode (as in **C**).

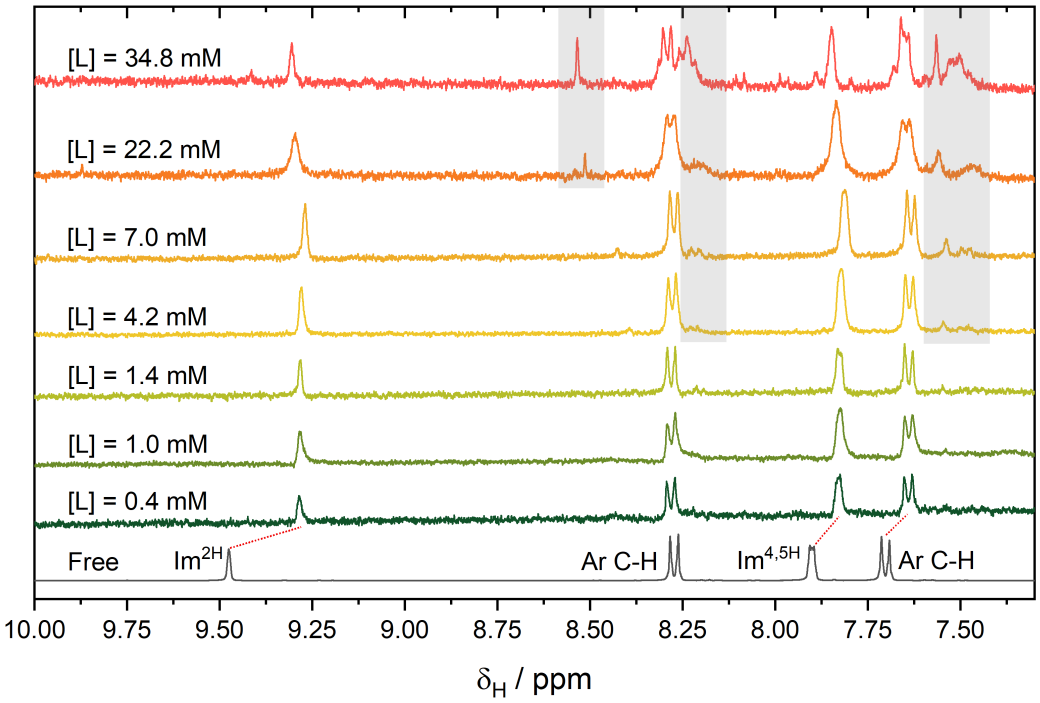

Figure S45. ^{1}H NMR of **Ag-3-NO$_2$** recovered in d_6-DMSO, showing the effect of the ligand concentration, [L], used in the exchange on the resulting spectra. Major shifts in the aromatic ligand ^{1}H resonances are highlighted with red dashed lines. Grey boxes highlight the appearance of the second set of ligand resonances.

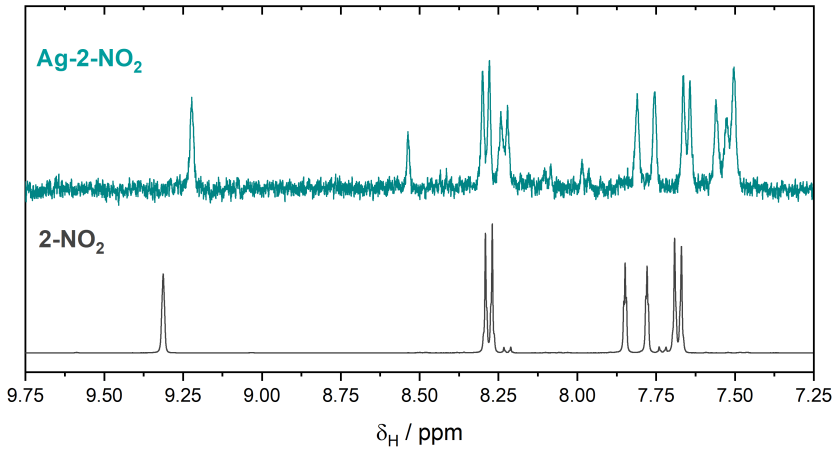

Figure S46. ^{1}H NMR spectra of **2-NO$_2$** and **Ag-2-NO$_2$** in d_6-DMSO, showing only the aromatic region for clarity. 8 scans were recorded for the free ligand and *ca*. 2000 scans for the hybrid AgNCs.

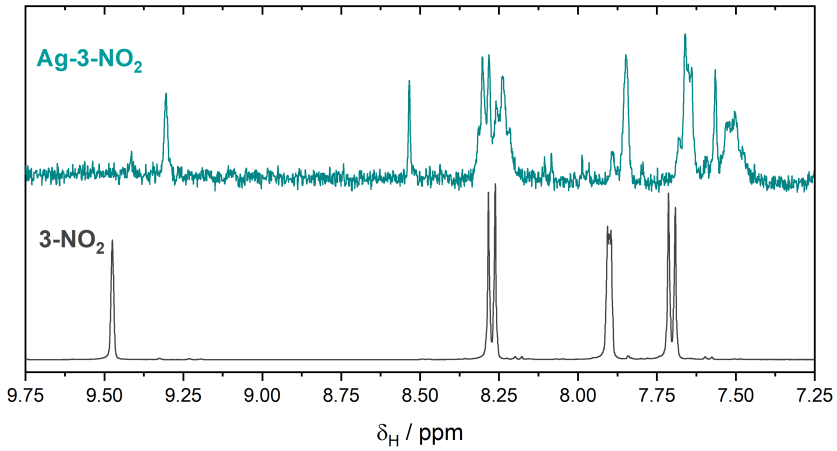

Figure S47. ^{1}H NMR spectra of **3-NO$_2$** and **Ag-3-NO$_2$** in d_6-DMSO, showing only the aromatic region for clarity. 8 scans were recorded for the free ligand and *ca*. 2000 scans for the hybrid AgNCs.

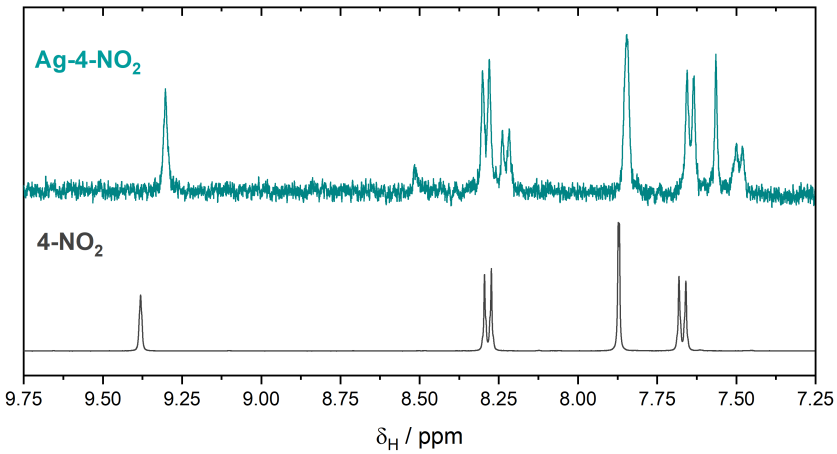

Figure S48. ^{1}H NMR spectra of **4-NO$_2$** and **Ag-4-NO$_2$** in d_6-DMSO, showing only the aromatic region for clarity. 8 scans were recorded for the free ligand and *ca*. 2000 scans for the hybrid AgNCs.

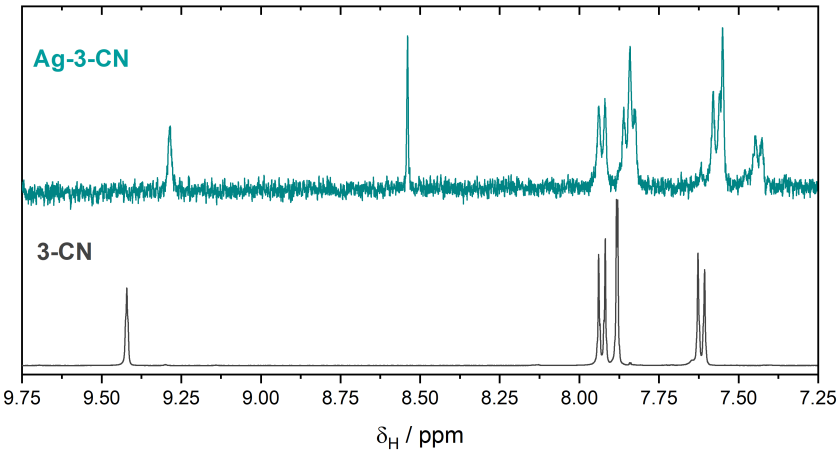

Figure S49. ^{1}H NMR spectra of **3-CN** and **Ag-3-CN** in d_6-DMSO, showing only the aromatic region for clarity. 8 scans were recorded for the free ligand and *ca*. 2000 scans for the hybrid AgNCs.

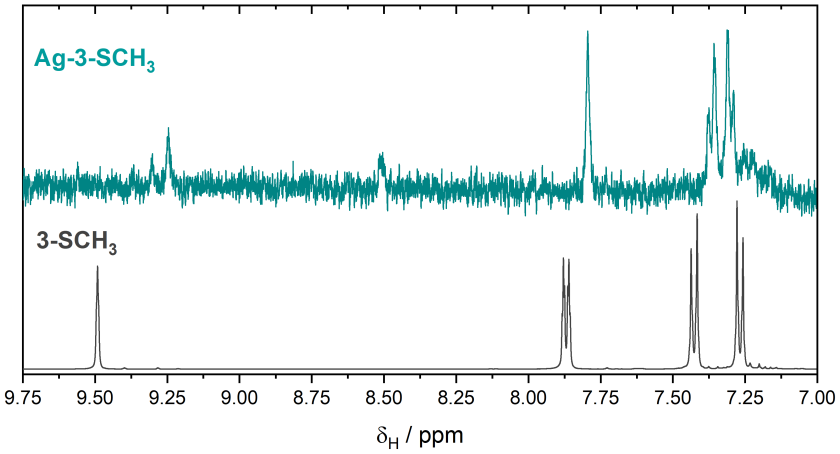

Figure S50. ^{1}H NMR spectra of **3-SCH$_3$** and **Ag-3-SCH$_3$** in d_6-DMSO, showing only the aromatic region for clarity. 8 scans were recorded for the free ligand and *ca*. 2000 scans for the hybrid AgNCs.

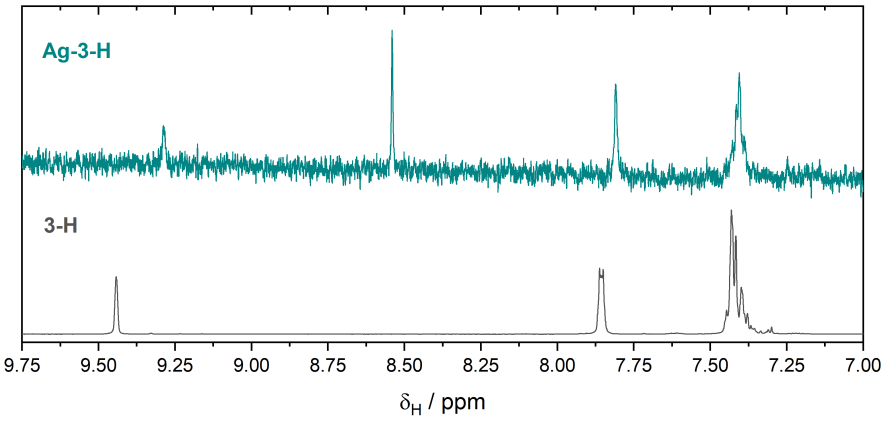

Figure S51. ^{1}H NMR spectra of **3-H** and **Ag-3-H** in d_6-DMSO, showing only the aromatic region for clarity. 8 scans were recorded for the free ligand and *ca*. 2000 scans for the hybrid AgNCs.

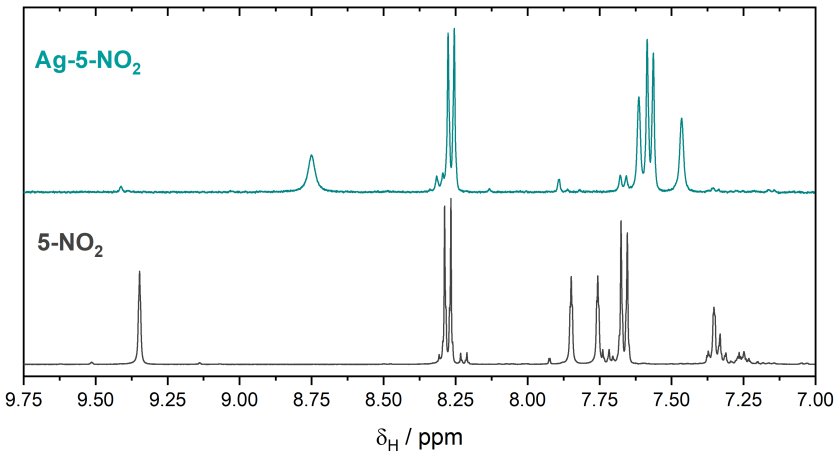

Figure S52. ^{1}H NMR spectra of **5-NO$_2$** and **Ag-5-NO$_2$** in d_6-DMSO, showing only the aromatic region for clarity. 8 scans were recorded for the free ligand and *ca*. 2000 scans for the hybrid AgNCs.

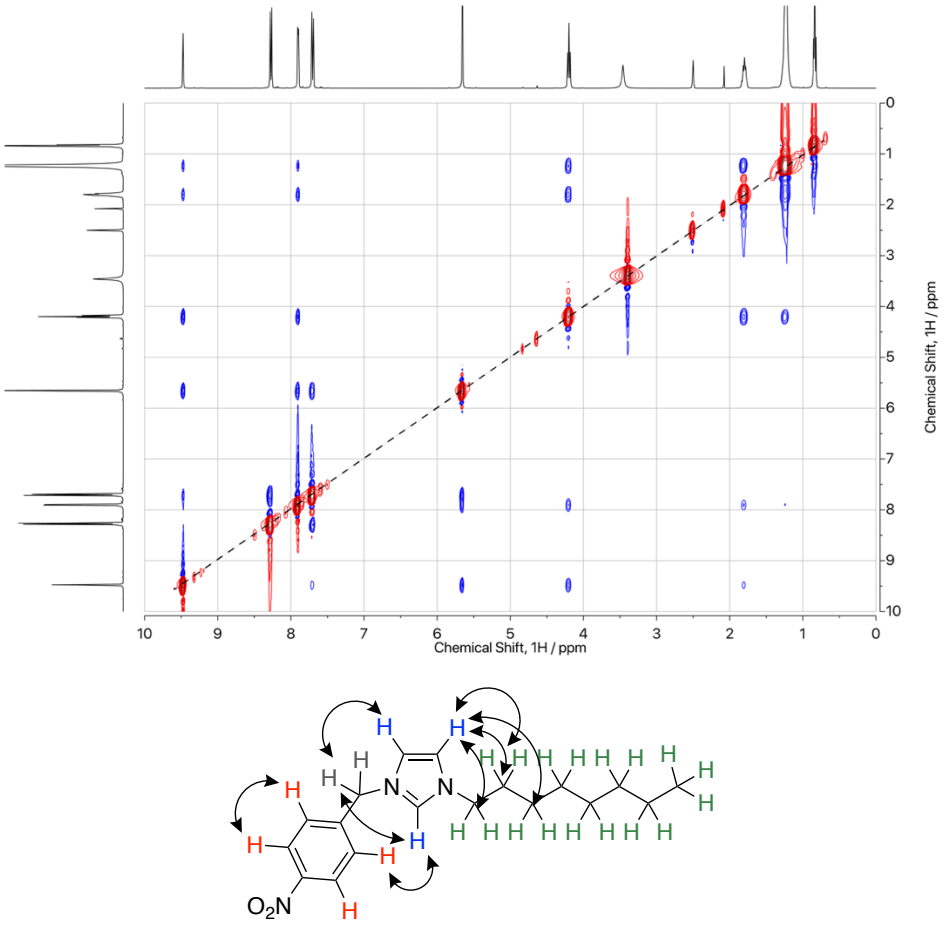

Figure S53. Top: ^{1}H-^{1}H NOESY spectrum of **3-NO$_2$**, measured in d_6-DMSO. The spectrum conforms to the determined structure and is included here to highlight how the diagonal and cross peaks are of different sign (red vs blue). Cross peaks are only observed between ^{1}H environments that are expected to be within *ca*. 3 Å in the molecule (through space). The red diagonal peaks are also highlighted with a dashed line. **Below**: schematic of NOESY interactions in **3-NO$_2$**.

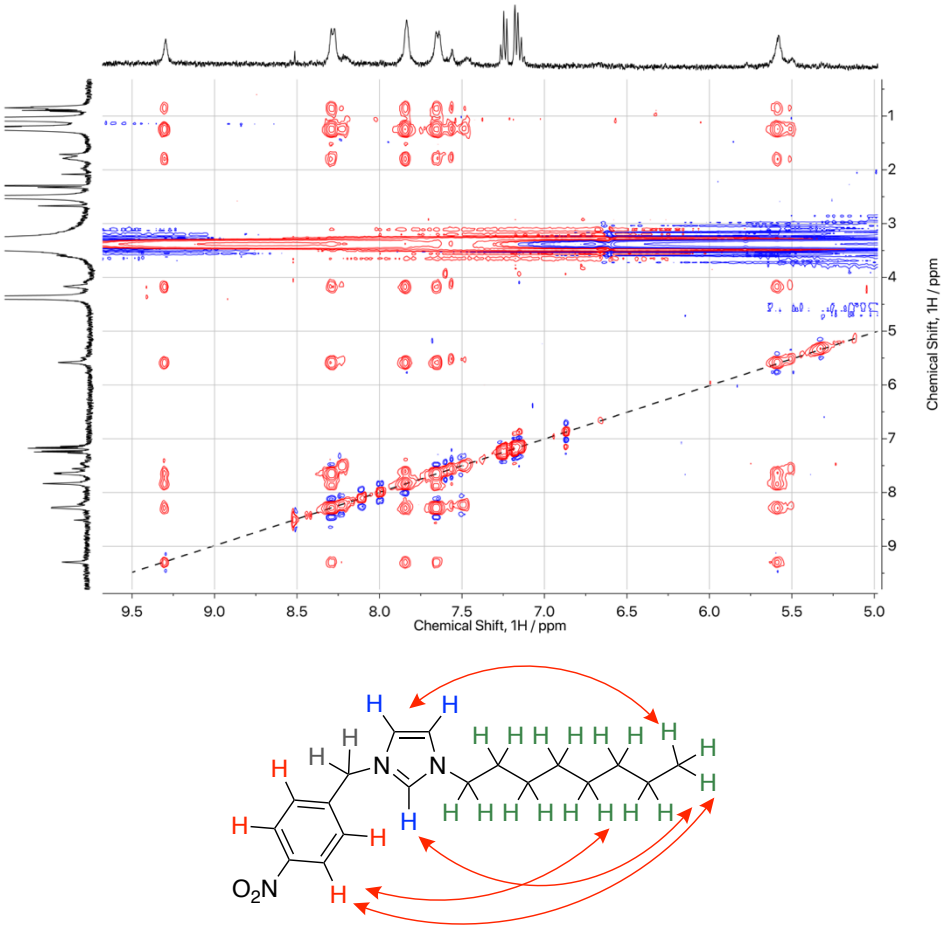

Figure S54. Top: ^{1}H-^{1}H NOESY spectrum of **Ag-3-NO$_2$**, measured in d_6-DMSO. In this case, the diagonal and cross peaks are all of the same sign (red), and there are a much greater number of NOESY interactions, between all ^{1}H environments in the ligand. The red diagonal peaks are highlighted with a dashed line. A zoomed view is given, as the alkyl region is dominated by the diagonal peak of water (seen here from the horizontal noise centred at 3.33 ppm). **Bottom**: NOESY interactions that are far longer than 3 Å, that are observed but should not be possible for a free ligand in solution. Such is a phenomenon observed for organic molecules on nanocrystal surfaces.[10]

Additional Electrochemical Data

Table S1. Average sample capacitance, surface area and current density values for Ag-OLAM and Ag-imidazolium hybrid catalysts. Current densities are given from experiments carried out at −1.1 V *vs* RHE using 14 µg Ag. Note that average J_{ECSA} and $J_{CO,ECSA}$ values were calculated from their respective individual values, not from the average J_{geom} and S values given in the table.

Ligand	C [a] / µF cm^{-2}	S [b] / cm^2	J_{geom} [c] / mA cm^{-2}	J_{ECSA} [d] / µA cm^{-2}	$J_{CO,ECSA}$ [e] / µA cm^{-2}
OLAM	362 ± 141	19.53 ± 7.61	–3.44 ± 0.71	–170 ± 34	–49 ± 18
1–NO$_2$	183 ± 7	9.89 ± 0.38	–2.42 ± 0.14	–367 ± 35	–233 ± 23
2–NO$_2$	160 ± 38	8.65 ± 2.04	–1.96 ± 0.11	–351 ± 75	–258 ± 55
3–NO$_2$	235 ± 35	12.70 ± 1.90	–2.37 ± 0.54	–277 ± 27	–256 ± 28
3b–NO$_2$	166 ± 6	8.94 ± 0.30	–2.36 ± 0.13	–395 ± 13	–275 ± 43
4–NO$_2$	274 ± 32	14.76 ± 1.74	–3.00 ± 0.40	–303 ± 38	–131 ± 30
5–NO$_2$	264 ± 31	14.23 ± 1.65	–1.62 ± 0.14	–172 ± 7	–139 ± 7
3–CN	164 ± 83	8.87 ± 4.49	–2.15 ± 0.13	–285 ± 197	–219 ± 27
3–CO$_2$H	285 ± 78	15.38 ± 4.20	–2.36 ± 0.46	–245 ± 22	–188 ± 18
3–SCH$_3$	285 ± 55	15.36 ± 2.99	–2.35 ± 0.20	–209 ± 52	–160 ± 40
3–H	66 ± 10	3.56 ± 0.54	–0.70 ± 0.01	–297 ± 38	–172 ± 22
4–CN	307 ± 71	16.58 ± 3.82	–3.06 ± 0.73	–277 ± 25	–131 ± 29
4–CO$_2$H	338 ± 126	18.24 ± 6.79	–3.42 ± 0.85	–295 ± 79	–120 ± 45
4–SCH$_3$	239 ± 1	12.91 ± 0.06	–3.47 ± 0.91	–403 ± 31	–112 ± 29
CTAB	287 ± 41	15.50 ± 2.21	–1.96 ± 0.34	–189 ± 14	–105 ± 11

[a] sample capacitance / µF cm^{-2}; [b] sample surface area / cm^2; [c] geometric current density for a 1.5 cm^2 electrode / mA cm^{-2}; [d] current density after normalization by the electrochemically active surface area / µA cm^{-2}; [e] partial current density for CO after normalization by the electrochemically active surface area / µA cm^{-2}.

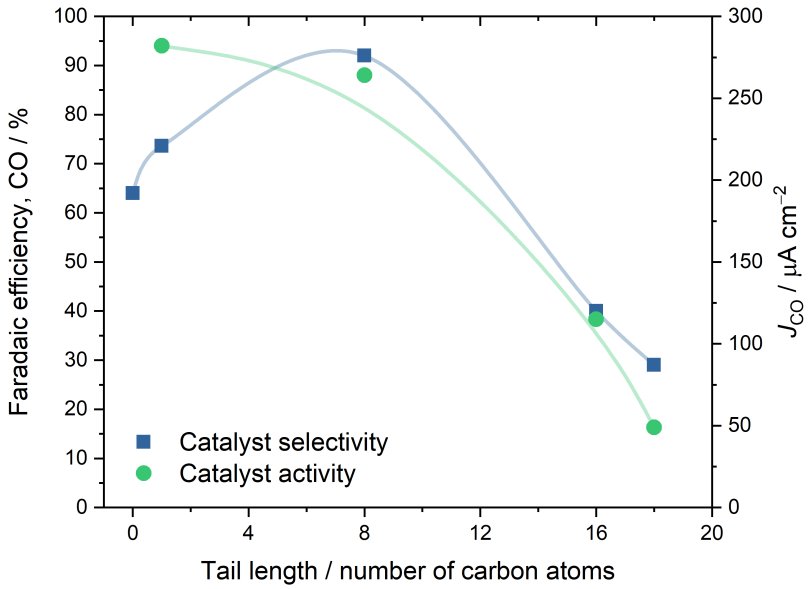

Figure S55. Correlations of the length of the linear hydrocarbon tail groups with CO_2RR selectivity and activity.

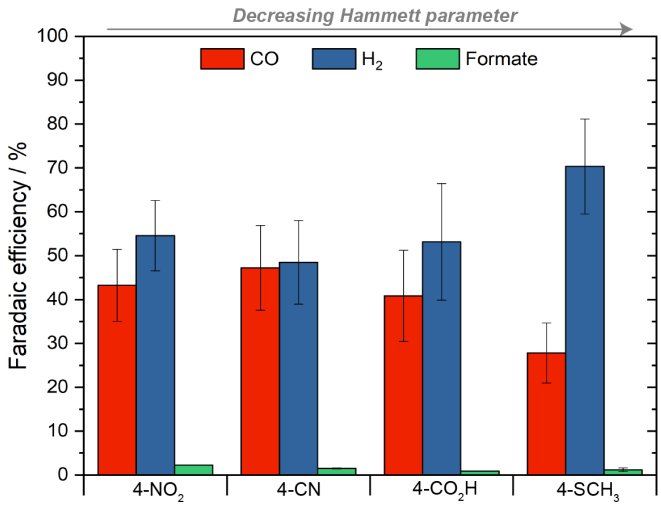

Figure S56. CO_2RR performance of hybrid AgNC catalysts bearing imidazolium ligands with hexadecyl tail groups, showing how the selectivity of these catalysts is poor, regardless of the anchor group. Error bars represent standard deviation taken from three independent measurements.

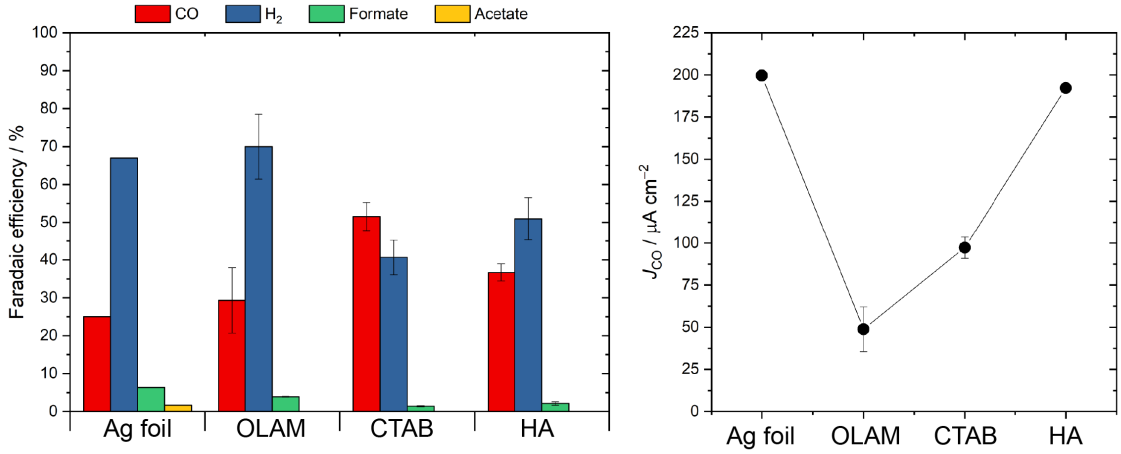

Figure S57. CO_2RR data from control experiments, where OLAM = oleylamine, CTAB = cetyltrimethyl ammonium bromide, and HA = n-hexylamine. **Left**: Selectivities, described by Faradaic efficiencies. **Right:** Activities, described by the partial current density for CO (normalised by the ECSA).

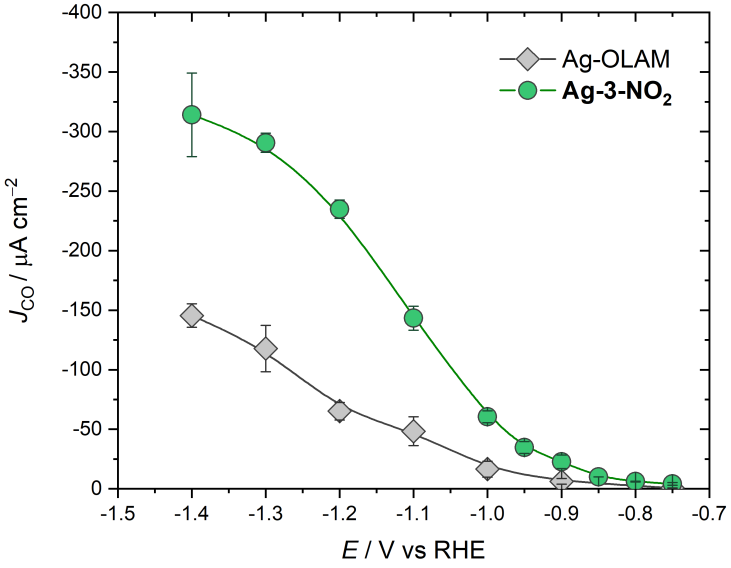

Figure S58. Partial current densities for CO, measured for **Ag-OLAM** and **Ag-3-NO_2** at various potential, showing an improvement in the CO_2RR overpotential for hybrid AgNCs.

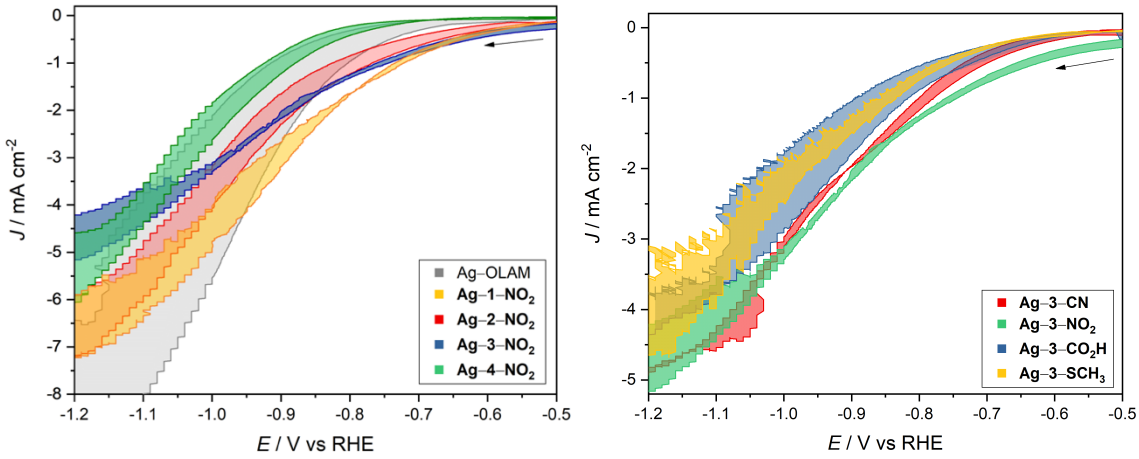

Figure S59. Linear-sweep voltammograms (LSVs) for OLAM-bearing AgNCs and new hybrid AgNCs, measured at a scan rate of 10 mV s^{-1} whilst sparging CO_2 gas through the electrolyte. LSV plots were made from three independent measurements and are reported as coloured bands using the minimum and maximum LSV traces as boundaries. Geometric current-densities are reported following normalisation by surface roughness (determined from capacitance measurements). **Left:** ligands with a common anchor group (NO_2) and varying tail groups are compared, along with the as-synthesized **Ag-OLAM** NCs as a reference. **Right:** ligands with a common tail group (*n*-octyl) and varying anchor groups are compared. Comparing current densities at −1 mA indicates a reduction of the onset potential by *ca*. 150 mV. We also observe that ligands with shorter tails and NO_2 groups in the anchor give the best reduction in the onset potential.

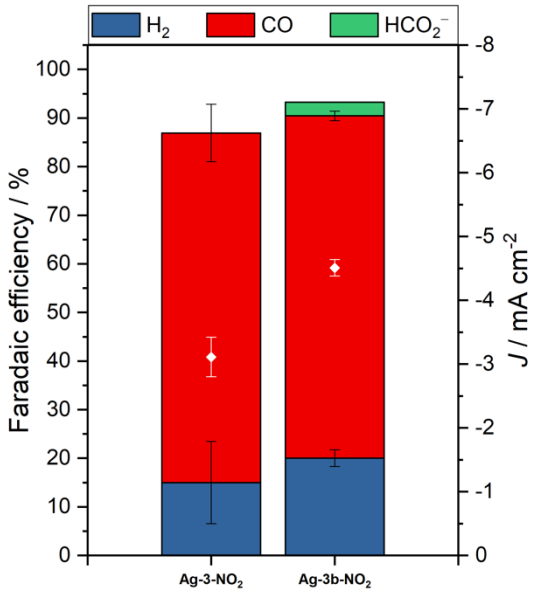

Figure S60. Performances of **Ag-3-NO_2** and **Ag-3b-NO_2** in the CO_2RR, showing the effect of blocking the imidazole 2-position with a methyl group. The applied potential was −1.1 V *vs* RHE and the mass loading of Ag was 14 µg; geometric current-densities are reported, which were normalized by surface roughness (white points). The near-equivalent performance for these two hybrid materials proves that deprotonation of the imidazole 2-position is not relevant to the reaction mechanism in this study.

XPS data and discussion on electronic structure

X-ray photoelectron spectra (XPS) were recorded for the free ligands and the hybrid NC films on Si. The presence of the imidazolium ligands on the AgNCs was confirmed from their characteristic C1*s*, N1*s*, O1*s*, S2*p* and Br3*p* peaks. For the C1*s* peak, a shoulder at higher binding energy implied a higher number of C–N double bonds in comparison with the **Ag-OLAM** precursor, in agreement with the introduction of multiple aromatic groups (data not shown). Similarly, the N1*s* peaks arising from mixtures of imidazolium, nitro or nitrile groups were all observed at higher binding energies in comparison with the amino N1*s* peak from OLAM, which was not observed at all in the hybrid NC films. In comparison with the free ligands, the N1*s* peaks in the hybrid AgNCs were also all shifted to lower binding energies. This is accompanied by a simultaneous shift of the Ag3*d* peaks to lower binding energies, which for Ag implies that the surface has become more electron poor.[12,13] From these observations we conclude that the imidazolium ligands are electron-withdrawing and pull electron density away from the Ag surface, which is most likely caused by the formal cationic charge on the imidazolium group. In agreement with this point, **Ag-1-NO2** was the only hybrid that featured a more electron-rich Ag surface, evident from the shift of its Ag3*d* peaks to higher binding energies; **1-NO2** is the only ligand studied that does not carry a formal positive charge.

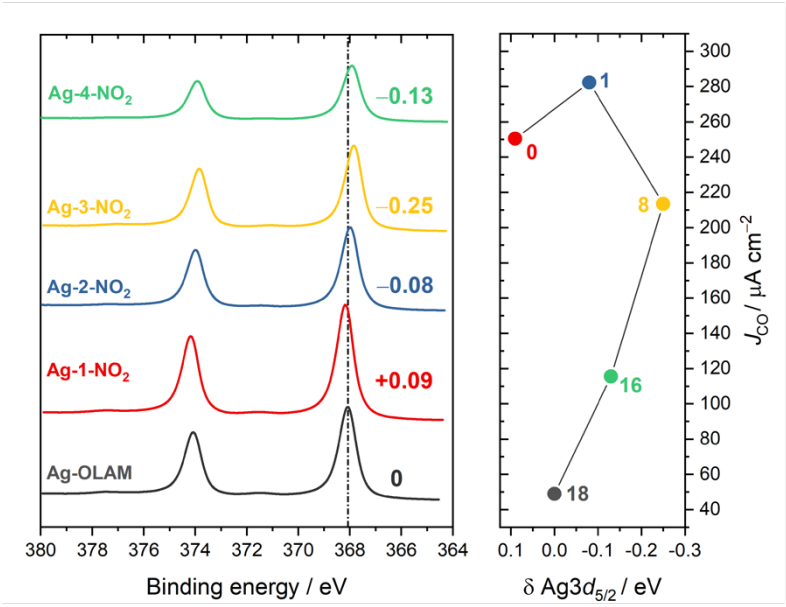

Figure S61. Left) Ag3*d* XPS spectra for **Ag-OLAM** and hybrid AgNCs, showing the effect of the tail length on the Ag electronic structure for NO_2-containing ligands. Shifts of the Ag3$d_{5/2}$ peaks are indicated. Note that there is no linear correlation of the tail length with the shift of the Ag3$d_{5/2}$ XPS peak. The dashed line marks the peak position of Ag-OLAM 3$d_{5/2}$. **Right**) Correlation of the shifts of these Ag XPS peaks with the corresponding catalytic performance, described by J_{CO}. Labels indicate the hydrocarbon tail length. Here too, there is no apparent correlation, from which we conclude the tail groups do not influence the CO_2RR due to electronic reasons.

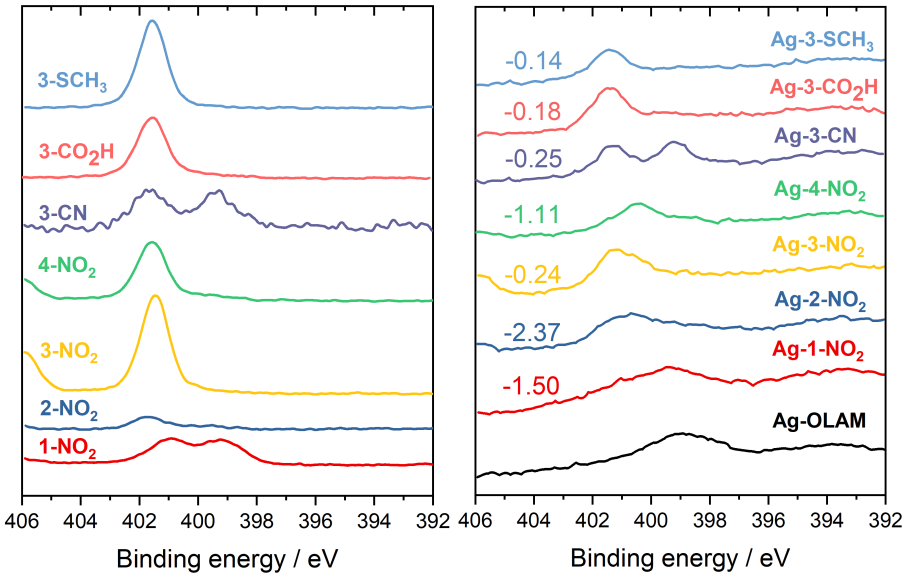

Figure S62. N1*s* XPS spectra of free ligands (left) and hybrid AgNCs (right); the numbers in the right-hand plot indicate the change of the imidazolium N1*s* peaks after being immobilized on the AgNC surface. In their free forms, **1-NO_2** shows two imidazole N1*s* peaks due to asymmetry in the monosubstituted imidazole, whereas **3-CN** shows two peaks due to the imidazolium N-atoms and the nitrile N-atom.

UV-vis Spectra

For **Ag-OLAM**, a typical surface plasmon resonance (SPR) peak was observed at 397 nm in hexane. The AgNC hybrids are in DMSO. The SPR peak is known to be sensitive to changes in the NC surface chemistry as well as the solvent polarity.[14,15] Specifically, the SPR peak is expected to red-shift in DMSO, which is what we observe for all the hybrids, except for **1-NO_2** which is the only charge-neutral compound. Taking this into account, while convoluted with the solvent effect, the red shift observed for all the other hybrids is consistent with the decreased electron density concluded by the NMR and XPS data.

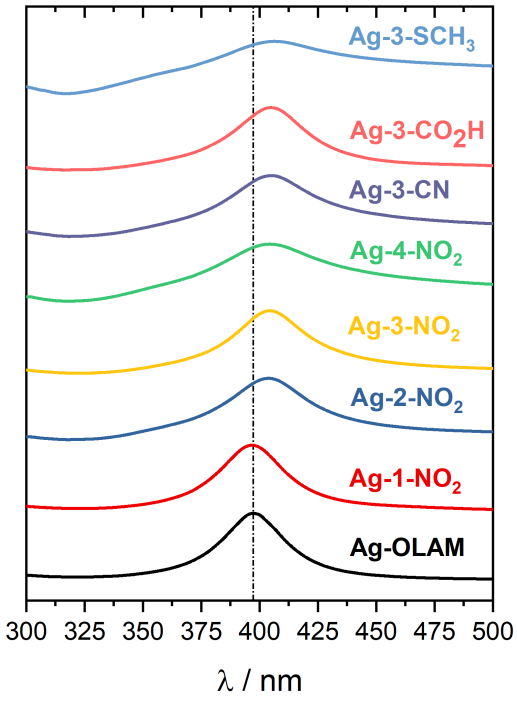

Figure S63. UV-vis absorption spectra for **Ag-OLAM** and hybrid AgNCs, measured as colloidal suspensions at room temperature. **Ag-OLAM** was measured in hexane, whereas the others were measured in DMSO. The dashed line marks the peak position of the SPR for **Ag-OLAM**.

Correlation of Ligand and Metal Electronic Structures

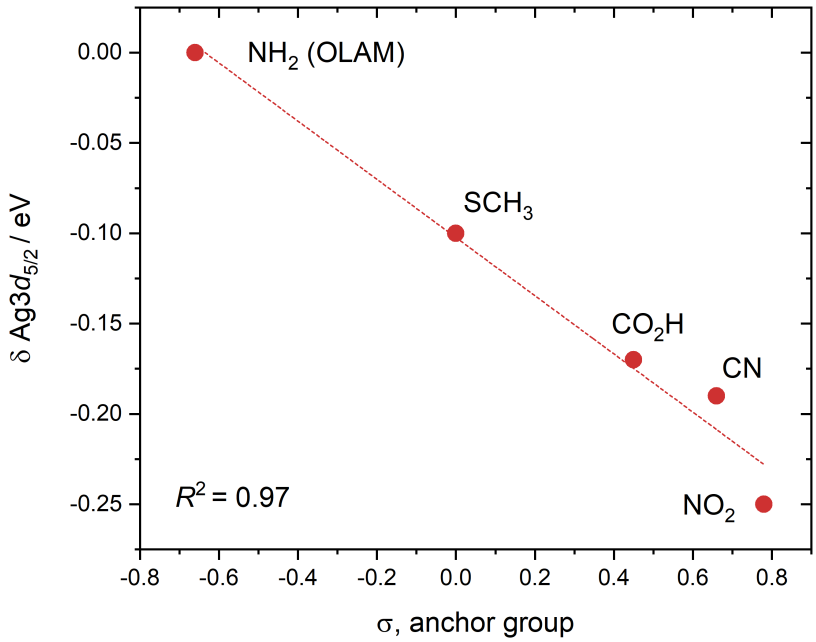

Figure S64. Correlation of the ligand anchor-group Hammett parameters against the XPS Ag3$d_{5/2}$ shifts for AgNCs. Whilst the amine group in OLAM is not an aryl substituent, we have used the Hammett parameter as a qualitative descriptor of the functional group.

Zeta-Potential Data

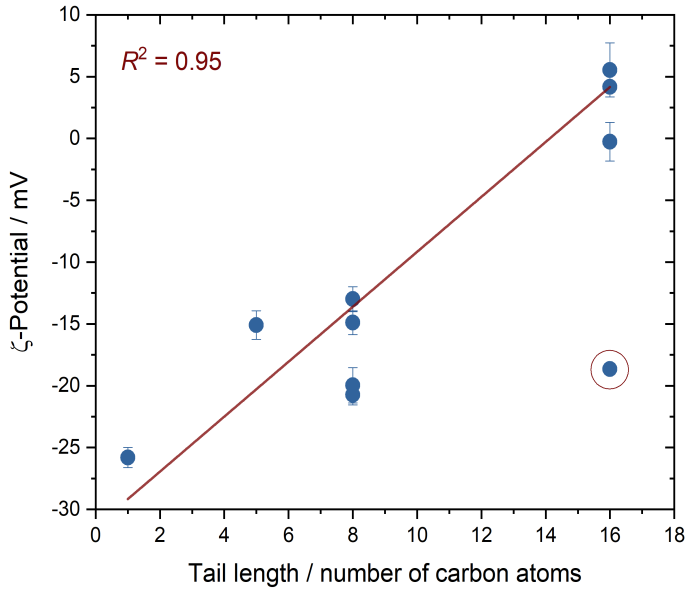

Figure S65. Correlation of ligand tail-length with the zeta-potential, measured in 0.1 M $KHCO_3$; **Ag-4-CO_2H** is circled as an obvious outlier from the trend and is not include in the fit.

Table S2. Zeta-potential values (ZP) measured in 0.1 M $KHCO_3$, showing average values from 3 measurements along with their standard deviations.

Ligand	ZP, 0.1 M $KHCO_3$ / mV
2-NO_2	−25.8 ± 0.8
3-NO_2	−20.7 ± 0.8
3-CN	−20.0 ± 1.4
3-CO_2H	−14.9 ± 1.0
3-SCH_3	−13.1 ± 1.0
4-NO_2	+5.5 ± 2.2
4-CN	−0.3 ± 1.6
4-CO_2H	−18.6 ± 0.2
4-SCH_3	+4.2 ± 0.1
5-NO_2	−15.1 ± 1.1

Post-electrocatalysis characterization of hybrid AgNCs

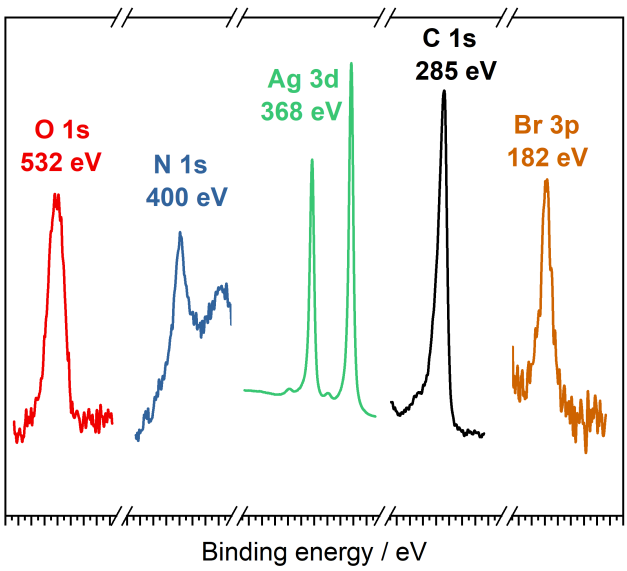

Figure S66. X-ray photoelectron spectra for **Ag-3-NO_2** following 1-hour CO_2RR electrolysis at −1.1 V *vs* RHE. After electrolysis, the catalyst film on glassy carbon was washed with deionized water and air-dried. The O1*s*, N1*s*, Ag3*d*, C1*s* and Br3*p* peaks for the ligand were all observed at similar positions as the pre-electrolysis sample.

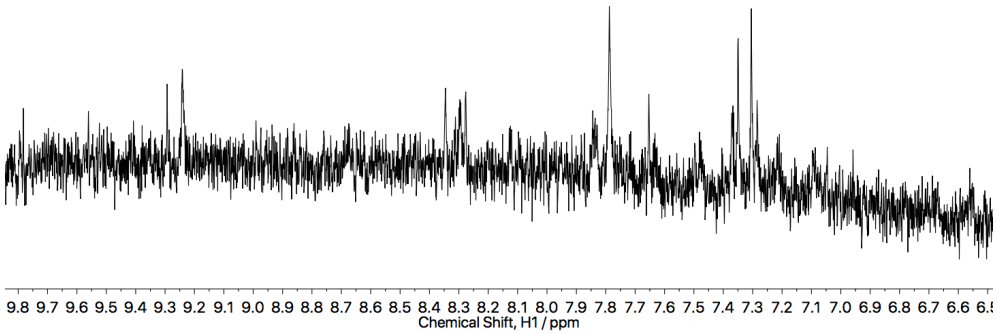

Figure S67. ^{1}H NMR spectrum of **Ag-3-NO$_2$**, recovered in d_6-DMSO following a 1-hour CO_2RR electrolysis experiment. For clarity, only the aromatic region is shown, where resonances for the 3-NO_2 ligand are observed. Number of scans = 2000. The low signal-to-noise ratio is due to the low concentration (40 μg Ag used in CO_2RR; volume of NMR solution = 500 μL).

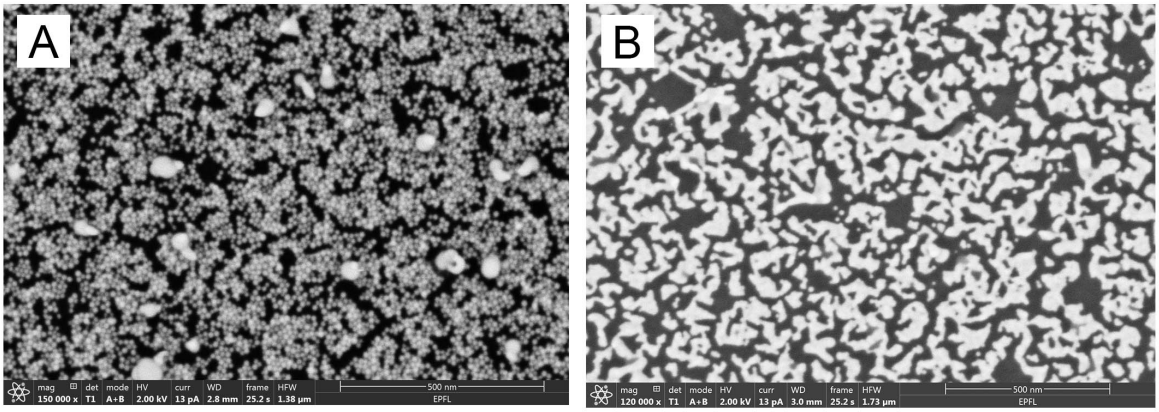

Figure S68. A) SEM image of **Ag-3-NO$_2$** pre-electrolysis, imaged directly on the glassy-carbon electrode. The mass loading of Ag was 14 μg. **B**) SEM image of **Ag-3-NO$_2$** following 85-minute electrolysis under CO_2RR conditions, imaged directly on the glassy-carbon electrode. The mass loading of Ag was 14 μg and the applied potential was −1.1 V *vs* RHE. The images show compositional contrast. From these images we can see that the hybrid AgNC catalysts begin as well-dispersed NCs but rapidly sinter into interconnected coral structures. The sintering occurs within the first 10 minutes of electrolysis.

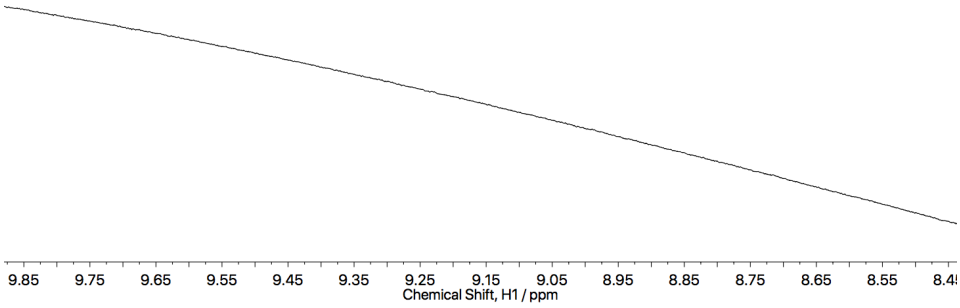

Figure S69. ^{1}H NMR spectrum of the catholyte (0.1 M $KHCO_3$, H_2O + 2 drops D_2O for spectrometer lock) following 1-hour CO_2RR electrolysis catalyzed by **Ag-3-NO$_2$**, showing a zoomed-in view of the aromatic region for clarity, where no resonances corresponding to free ligand were observed. Number of scans = 2000.

References

[1] A. Wuttig, Y. Surendranath, *ACS Catal.* **2015**, *5*, 4479–4484.

[2] Z. Xi, F. Liu, Y. Zhou, W. Chen, *Tetrahedron* **2008**, *64*, 4254–4259.

[3] E. Díez-Barra, A. de la Hoz, A. Sánchez-Migallón, J. Tejeda, *Synth. Commun.* **1993**, *23*, 1783–1786.

[4] K. Yamamoto, T. Kitayama, N. Ishida, T. Watanabe, H. Tanabe, M. Takatani, T. Okamoto, R. Utsumi, *Biosci. Biotechnol. Biochem.* **2000**, *64*, 919–923.

[5] K. Luerssen, U. Holtschmidt, G. Schwarzmann, *Mittel Zur Regulierung Des Pflanzenwachstums*, **1978**, DE2706838 A1.

[6] H. Giesemann, G. Hälschke, *Chem. Ber.* **1959**, *92*, 92–98.

[7] S. Semwal, I. Mukkatt, R. Thenarukandiyil, J. Choudhury, *Chem. – Eur. J.* **2017**, *23*, 13051–13057.

[8] C. Battocchio, F. Porcaro, S. Mukherjee, E. Magnano, S. Nappini, I. Fratoddi, M. Quintiliani, M.V. Russo and Giovanni Polzonetti, *J. Phys. Chem. C*, 2014, **118**, 8159

[9] K. Salorinne1, S. Malola, O.A. Wong, C.D. Rithner, X. Chen, C.J. Ackerson and H. Häkkinen, *Nat. Commun*., 2016, **7**, 10401

[10] Z. Hens and J.C. Martins, *Chem. Mater*., 2013, **25**, 1211-1221

[11] D. Neuhaus and M. Williamson, *The Nuclear Overhauser Effect in Structural and Conformational Analysis*, Wiley-VCH, New York, 2000

[12] S. K. Sengar, B. R. Mehta, Govind, *J. Appl. Phys.* **2014**, *115*, 124301.

[13] I. A. Abrikosov, W. Olovsson, B. Johansson, *Phys. Rev. Lett.* **2001**, *87*, 176403.

[14] J. Wei, N. Schaeffer, M.-P. Pileni, *J. Phys. Chem. B* **2014**, *118*, 14070–14075.

[15] S. K. Ghosh, S. Nath, S. Kundu, K. Esumi, T. Pal, *J. Phys. Chem. B* **2004**, *108*, 13963–13971.